

Highly Efficient Photocatalytic Degradation of Imidacloprid Based on Iron Metal–Organic Frameworks of Mesoporous NH₂-MIL-88b/Graphite Carbon Nitride Nanocomposites by Visible Light Driven in Aqueous Media

Elham Chiani, Shahram Ghasemi,* and Seyed Naser Azizi



Cite This: *ACS Omega* 2024, 9, 26983–27001



Read Online

ACCESS |



Metrics & More



Article Recommendations



Supporting Information

ABSTRACT: Pesticides that protect crops from insects and other pests are some of the main causes of water pollution. Imidacloprid (IMC) is the most widely used insecticide in the world and should be removed from the environment. This work aims to prepare mesoporous nanocomposites to increase the photodegradation efficiency of IMC. To improve the surface properties and enhance the photocatalytic activity, mesoporous nanocomposites with different weight ratios of graphite carbon nitride (CN = 125, 250, and 500 mg) were prepared by the solvothermal method. Mesoporous NH₂-MIL-88b(Fe)/graphite carbon nitride (CN = 250 mg, NH₂-MCN-2) nanocomposites showed the best photocatalytic performance. To save the time and cost of the experiments, central composite design (CCD) and response surface methodology (RSM) were used and the results were obtained as the initial concentration of IMC (20 mg L⁻¹), amount of photocatalyst (0.76 g L⁻¹), pH = 5, and degradation time ~46 min. The maximum photocatalytic degradation efficiency estimated by the model was obtained at 96.31%, which is very close to the actual value of 95.47%. The mesoporous NH₂-MCN-2 nanocomposite showed excellent stability and suitable reusability with a maximum degradation of 84.5% after five cycles. Results obtained from kinetic studies indicated a rate constant value of 0.08 min⁻¹, and isotherm models showed that equilibrium data are more consistent with the Langmuir model in photocatalytic degradation. Electrochemical experiments showed significant improvement in the electron transfer rate and photocatalytic activity of the mesoporous NH₂-MCN-2 nanocomposite. Different trapping agents were used to investigate the effective active species in IMC photodegradation, and it was determined that the hole (h⁺) and OH radical (•OH) play the main role. The possible mechanism for IMC photocatalytic degradation was suggested by Mott–Schottky (M-S) electrochemical impedance.



1. INTRODUCTION

Pesticides are chemicals used to control weeds and harmful insects.¹ Although the use of insecticides and herbicides in the production of agricultural products increases the yield and improves the quality of farm products, they have destructive effects that cannot be ignored.²

Based on the results of research, imidacloprid (IMC) is considered one of the most dangerous insecticides for the environment,³ and among the top 10 global agrochemicals, it is ranked second.⁴ IMC is extensively utilized for pest control in agriculture, gardens, and lawns, foundations to prevent termite damage, flea control in domestic dogs,⁴ protecting trees from boring insects,³ etc. IMC decomposes very slowly in the dark at pH between 5 and 7, and its half-life at pH = 9 is about 1 year; therefore, it remains in underground water for a long time. The stability of IMC in soil under aerobic conditions is 1 to 3 years with a half-life of 39 days on the soil surface. Due to

the high use of IMC, it usually enters the water flow as a spray drift or runoff after use and its high solubility in water (0.61 g L⁻¹)⁵ remains stable approximately between 30 and 50 days, making it a severe pollutant for water. This insecticide is a neonicotinoid that disrupts the transmission of stimuli in the nervous system of insects. IMC poses severe threat to human life in addition to its killing effect on insects.⁶ It causes severe damage to human skin and eyes.⁴ Also, the effects of poisoning with IMC can be seen in the form of fatigue, irritability,

Received: December 22, 2023

Revised: April 12, 2024

Accepted: May 31, 2024

Published: June 12, 2024



diarrhea, and muscle weakness, especially in the respiratory muscles.⁷

Various methods, such as microbial decomposition,⁸ adsorption,⁹ electrochemistry,¹⁰ ozonation,¹¹ and advanced oxidation processes (AOPs),¹² have been used to remove poisons from the aquatic environment. AOPs are one of the most effective methods in the decomposition of resistant pollutants, which have received much attention in recent years. Active species of hydroxyl and sulfate radicals have high reactivity due to having free electrons. AOP is widely used in wastewater treatment for the degradation of various pollutants with complex and rigid structures that are not quickly and completely decomposed by conventional methods. This process has very high power in material degradation such as aromatic compounds, petroleum, organic and inorganic materials with strong bonds, etc. After complete degradation by AOP, these pollutants turn into harmless compounds such as H₂O and CO₂.

Recently, the use of efficient photocatalysts based on visible light has received particular attention for water purification. Graphite carbon nitride (g-C₃N₄), which is a metal-free semiconductor, has a structure similar to that of graphene. This structure is used for various applications such as reducing carbon dioxide,¹³ water splitting,¹⁴ and degrading pollutants.¹⁵ g-C₃N₄ is a photocatalyst with a suitable energy gap (ca. 2.7 eV)¹⁴ that responds to visible light. Its advantages include nontoxicity, chemical stability, simple fabrication method, easy preparation from available raw materials, and high solar absorption. However, g-C₃N₄, due to its low specific surface area, exhibits low performance in practical applications. To decrease the rate of recombination of the produced charge carriers (electron–hole pair), improve sensitivity to light, increase stability, and as a result, increase the activity of its photocatalyst, the use of approaches such as connecting with other semiconductors, doping, loading with a co-catalyst, utilization of ionic and non-ionic surfactants, and preparation of various composites with compounds like metal–organic frameworks (MOFs), has been studied.¹⁶

On the other hand, the research in recent decades shows the widespread use of MOFs as photocatalysts for the degradation of pollutants in aqueous environments.¹⁵ MOFs are crystal structures that are formed by the connection of metal ions and organic ligands. These frameworks have a unique design capability, and it is easy to synthesize and achieve different physicochemical properties and pore size by changing the ligand or the central metal. Although active carbon and zeolites have a high surface area, a tiny dead volume in MOFs has made them more porous than active carbon and zeolites.¹⁷

Also, the use of prefunctionalized MOFs with additional functional groups such as amine and hydroxyl has received much attention. Among the vast family of MOFs, MIL-88 (Lavazier Institute materials) has a high absorption capacity due to its large pore volume. Its high chemical and thermal stability has made it widely used in various processes.^{18,19} In particular, amine-doped MOFs have a high affinity for acid gas molecules and active sites for catalysis.²⁰ NH₂-MIL-88b (Fe) is a subset of MIL compounds introduced to heterogeneous photocatalytic systems due to its high surface area, unsaturated metal sites, specific pore size, and amine groups to improve light absorption.

It is expected that MOF/g-C₃N₄ composites improve photocatalytic activity by increasing the surface area and reducing the recombination rate of photogenerated charges.

For example, in NH₂-MIL-101(Fe)@C₃N₄, an efficient transfer of photogenerated charge carriers between the constituent components of the composite can be observed; because of these properties, the photocatalyst can be used in photodegradation of many kinds of organic and inorganic pollutants. Zhao et al. proposed the photocatalytic mechanisms for the reduction of Cr(VI) and oxidation of bisphenol A by NH₂-MIL-101(Fe)/C₃N₄.²¹ The introduction of g-C₃N₄ into NH₂-MILbase on Fe increased both light absorption and interfacial charge carrier separation.^{22–24}

Experimental design includes mathematical techniques used for statistical modeling and systematic analysis.²⁵ The response surface methodology (RSM) in experimental design is superior to the customary time-consuming approach of one variable at a time due to the reduction in the number of experiments, the increase in speed, and the systematicity of processing variables.^{26,27} Box–Wilson's second-order central compound design (CCD) is an efficient and RSM standard design that has attracted many researchers' attention; for example, Kumar et al. used the CCD approach to optimizing the separation of leukemic acid by reactive components.²⁸ Sarai et al. evaluated and optimized the effect of various factors on total organic carbon (TOC) degradation using the RSM based on CCD.²⁹

In recent decades, MOFs as a new category of porous materials have found a good perspective in the preparation of composites for photocatalytic applications due to their high structural diversity and suitable energy gap in the visible region. Among the large number of reported structures, MOFs based on carboxylate ligands and high-valent metal ions such as Fe (III) have attracted the attention of many researchers due to their unique physical and chemical properties.

One of the important factors in reducing the rate of recombination of charge carriers produced in the photocatalytic process is the surface area of the photocatalyst. As the surface area increases, the recombination rate decreases. Since g-C₃N₄ has a high recombination rate, forming a composite with NH₂-MIL88b (Fe) with its appropriate specific surface area leads to a higher surface area compared to g-C₃N₄ alone and improves the photocatalytic performance. As the specific surface area of mesoporous nanocomposites increases, the recombination rate decreases compared to g-C₃N₄ alone.

For this purpose, in this work, for the first time, mesoporous nanocomposites based on iron-MOF and amine-functionalized carboxylate ligand, which is an effective structural block, were studied with g-C₃N₄ for efficient photocatalytic degradation of IMC from aqueous solutions. Mesoporous NH₂-MCN nanocomposites were synthesized by the solvothermal method by introducing various weight ratios of g-C₃N₄ (CN = 125, 250, and 500 mg). Among these different composites, NH₂-MIL-88b(Fe)/graphite carbon nitride (CN = 250 mg, NH₂-MCN-2) showed the best photocatalytic performance due to its higher specific surface area and lower energy gap. In the following, the statistical method of CCD was used to measure the effects of different factors. With RSM, the impact of the independent variables on the response was examined with suitable optimum conditions. Typically, a 20 mg L⁻¹ (ppm) IMC solution was degraded up to 95.47% by the mesoporous NH₂-MCN-2 nanocomposite. NH₂-MCN-2 showed excellent stability and reusability for five recycling cycles under the same experiment conditions. In the following, the kinetics of the reaction was investigated by pseudo-first-order and pseudo-second-order models. In addition, the Langmuir, Freundlich, Temkin, and Dubinin–Radushkevich adsorption isotherm

models were also studied. Electrochemical impedance spectroscopy (EIS) and photocurrent responses of mesoporous NH₂-MCN-2 nanocomposites, NH₂-MIL-88b(Fe), and g-C₃N₄ were also reviewed. A significant improvement in the electron transfer rate and photocatalytic activity of NH₂-MCN-2 compared to g-C₃N₄ and NH₂-MIL-88b(Fe) was observed. To investigate the effective reactive species in the photodegradation process of IMC, different trapping agents were used, and the efficient role of h⁺ and •OH in the photodegradation process was determined. The proposed mechanism was investigated based on the results achieved from M-S electrochemical impedance.

2. EXPERIMENTAL SECTION

2.1. Chemicals and Reagents. Urea (CH₄N₂O, >99%), iron trichloride hexahydrate (FeCl₃·6H₂O, ≥97%), sodium sulfate (Na₂SO₄, >99.5%), potassium hexacyanoferrate (III) (K₃Fe(CN)₆, >99%), potassium hexacyanoferrate (II) (K₄Fe(CN)₆, >99%), potassium chloride (KCl, >99.5%), methanol (CH₃OH, 98%) and ethanol (C₂H₅OH, 98%) were supplied from Merck. 2-Aminoterephthalic acid (NH₂-BDC, 99%), N,N'-dimethylformamide (DMF, ≥99%), imidacloprid (IMC, ≥98%), ammonium oxalate (AO, >99%), isopropyl alcohol (IPA, ≥99.5%), 1,4-benzoquinone (BQ, ≥97%), and silver nitrate (AgNO₃, ≥99%) were purchased from Sigma-Aldrich.

2.2. Preparation of g-C₃N₄, NH₂-MIL-88b(Fe), and Mesoporous NH₂-MCN Nanocomposites. g-C₃N₄ was synthesized through thermal polycondensation of urea. Ten grams of urea was heated in an alumina crucible with a cover at a rate of 10 °C min⁻¹ to 550 °C and then calcined at this temperature for 3 h in an ambient air atmosphere. After natural cooling to room temperature, a light yellow powder product was obtained and used for the synthesis of composites.

Using a thermal solvent process, iron salt (FeCl₃·6H₂O) and NH₂-BDC were used as a ligand to bind to iron sites for the synthesis of NH₂-MIL-88b(Fe) with a hexahedral structure. For this purpose, 0.74 g of iron salt was dissolved with 0.25 g of H₂BDC in 30 mL of DMF, subjected to ultrasonic waves for 30 min, and then heated in a stainless steel autoclave with Teflon coating for 24 h at a temperature of 110 °C. The obtained product was naturally cooled to room temperature, then washed with methanol, and dried in vacuum at 60 °C for 12 h. After grinding, reddish-brown dry powder NH₂-MIL-88b(Fe) was obtained.

Mesoporous NH₂-MCN nanocomposites were prepared by a solvothermal method. Different weight ratios of g-C₃N₄ (CN = 125, 250, and 500 mg) were added to 30 mL of DMF and ultrasonicated for 30 min. Then, 0.25 g of NH₂-BDC and 0.74 g of FeCl₃·6H₂O were added to the above solution, and the mixture was ultrasonicated for another 30 min. The solution was then added to a 100 mL Teflon-lined stainless steel autoclave and heated in an oven at 110 °C for 24 h. After the reaction, the product was separated by a centrifuge, washed several times with methanol, and finally dried in a vacuum oven at 60 °C for 12 h. Final products were labeled according to the weight ratios of g-C₃N₄ in mesoporous nanocomposites as NH₂-MCN-1, NH₂-MCN-2, and NH₂-MCN-3, respectively.

2.3. Characterization. An advanced X-ray diffractometer D8 (XRD, Philips PW1730) with a scanning speed of 0.05°/s and Cu Kα radiation (λ = 1.5405 Å) was utilized to determine the crystal structure of the samples. Fourier transform infrared (FT-IR, Bruker-Vector 22) spectroscopy was obtained using a spectrometer. Weight and atomic percentage, distribution of

catalyst elements, and morphology were measured using energy-dispersive X-ray spectroscopy (EDX/MAP, ZEISS Sigma 300) and field emission scanning electron microscopy (FE-SEM, ZEISS Sigma 300). The structural studies of the materials were carried out with transmission electron microscopy (TEM, Philips EM 208S, 100 kV). N₂ physisorption measurements (mini PROSLEB 100) were done at 77 K. The specific surface area was determined from the Brunauer–Emmett–Teller (BET) method, and the Barrett–Joyner–Halenda (BJH, mini PROSLEB 100) method was performed to determine the pore size distribution and volume. Thermogravimetric analysis (TGA, STA6000) was carried out under N₂ gas with a heating rate of 10 °C min⁻¹. Zeta potential analysis (Zeta SZ-100z) was utilized to determine the electric charge of particles. UV–vis diffuse reflectance spectroscopy (DRS, SCINCO, S-4100) and dual-beam optical spectroscopy (UV–vis, T90+ PG) were performed to record data. For recording steady-state photoluminescence (PL), a fluorescence spectrometer (PL, FP-8300 JASCO) was used. Nuclear magnetic resonance (NMR, Bruker ULTRASHIELD 400 AVANCE III) was registered. X-ray photoelectron spectroscopy (XPS, SPECS UHV) analysis was utilized to determine the chemical composition and type of bond on the surface of the sample as well as the possibility of identifying and determining the number of elements.

High-performance liquid chromatography (HPLC, Waters 1525) equipped with a UV detector (Waters 2487) and a column C18 (250 × 4.6 mm, 5 μm) was used with mobile phase acetonitrile/water (70:30, V/V) at a flow rate of 1.0 mL min⁻¹. Electrochemical impedance spectroscopy (EIS) and Mott–Schottky (M-S) electrochemical impedance experiments were carried out using a potentiostat/galvanostat (IRASOL) with a standard three-electrode cell containing platinum wire as a counter electrode, Ag/AgCl/KCl (3M) as the reference electrode, and glassy carbon electrode (GCE) as the working electrode (internal diameter, 2 mm). For this purpose, the open circuit potential (OCP) was used by applying a disturbance amplitude of 5 mV, and the frequency was swept from 100 kHz to 1 Hz.

2.4. Investigation of Photocatalytic Activity. Photocatalytic experiments for the degradation of IMC were carried out in a box with dimensions of 40 × 40 × 40 cm, containing a source of visible light radiation, and in a two-shell Pyrex glass cylindrical reactor with a capacity of 100 mL (inner diameter, 7 cm; height, 20 cm). The reaction medium was cooled to ambient temperature by circulating water using a circulator to maintain the temperature. Artificial radiation (λ > 400 nm) was supplied by a 300 W halogen lamp. The UV light-locking filter was placed on top of the reactor. In each step, 15 mg of mesoporous NH₂-MCN nanocomposites with various weight ratios was added to 50 mL of the IMC solution with a concentration of 30 mg L⁻¹. At first, the mixture was stirred in the dark for 15 min to equilibrate the absorption of IMC before irradiation, and then irradiation was carried out for 60 min. The distance between the source of radiation and the reactor was retained at 10 cm in all measurements. At certain time intervals of irradiation, a 3 mL IMC solution was coming out from the reactor and was centrifuged, and finally, the absorption of IMC solution was measured after passing through a syringe filter with dimensions of 0.45 μm using a UV–vis spectrophotometer at λ_{max} ~ 270 nm. The photocatalytic degradation efficiency (%R) and IMC adsorption

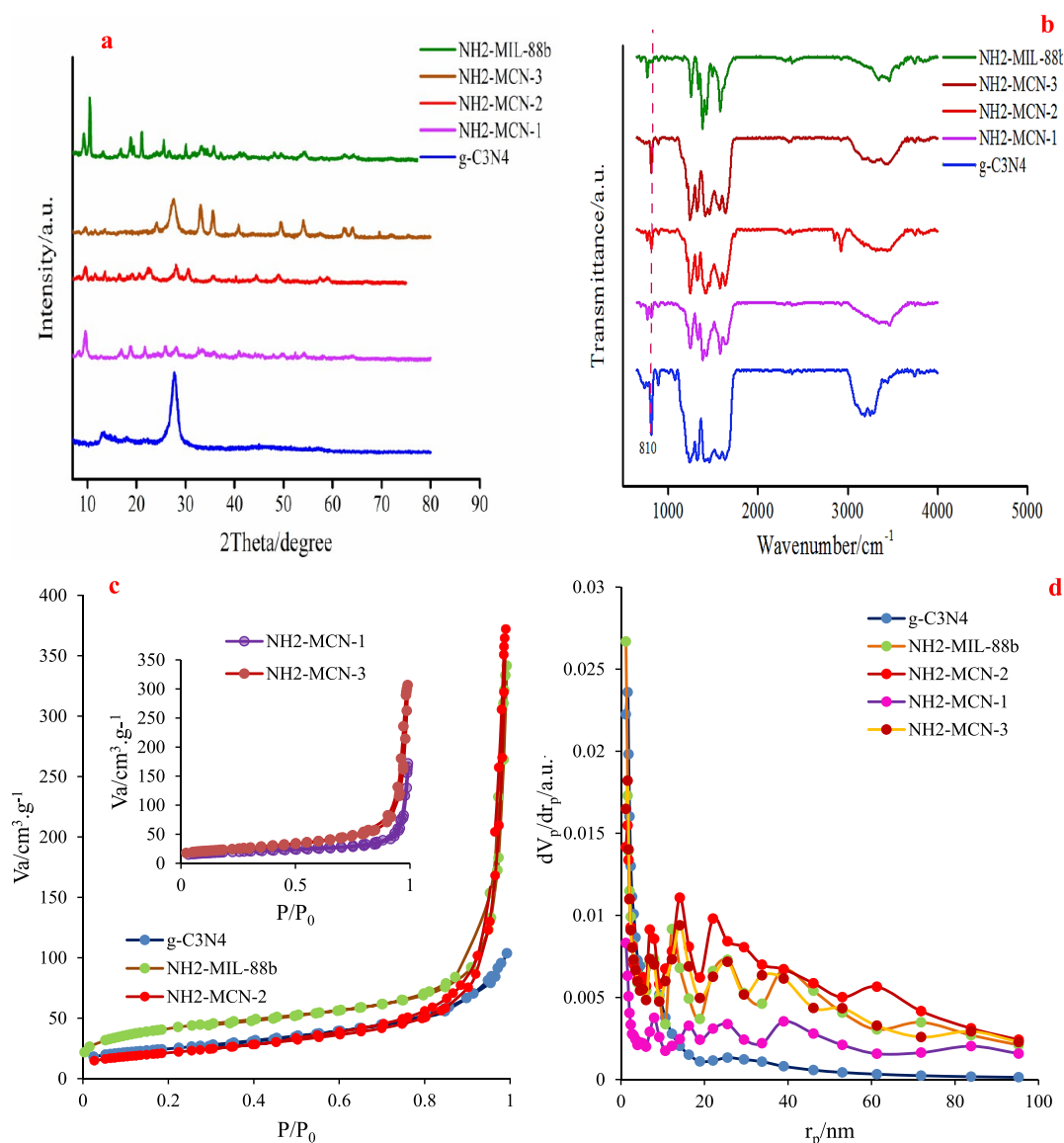


Figure 1. (a) XRD patterns, (b) FT-IR spectra, (c) N₂ adsorption–desorption isotherm, and (d) BJH of g-C₃N₄, NH₂-MIL-88b(Fe), and mesoporous NH₂-MCN nanocomposites with different weight ratios.

capacity (q_e) on mesoporous NH₂-MCN nanocomposites were calculated according to eqs 1 and 2, respectively:

$$\%R = \left(\frac{C_i - C_e}{C_i} \right) \times 100 \quad (1)$$

$$q_e = (C_i - C_e) \frac{V}{M} \quad (2)$$

where C_i and C_e are the initial concentration and equilibrium concentration of IMC in the solution, respectively, V is the volume of the solution (L), and M is the mass of the photocatalyst (g).

2.5. Photoelectrochemical and Electrochemical Experiments. For photoelectrochemical studies, 3 mg of the mesoporous NH₂-MCN-2 nanocomposite, NH₂-MIL-88b(Fe), and g-C₃N₄ was ultrasonically placed in 1 mL of DMF for 30 min to obtain slurry. Then, 100 μ L of a slurry was spread on a fluorine–tin oxide surface (FTO, 1 \times 1 cm) and dried at 60 $^{\circ}$ C for 30 min. The photocurrent responses of the photocatalysts were measured at OCP under visible light ($\lambda > 400$ nm) using

a potentiostat/galvanostat (Auto Lab 302 N) and in a solution (0.5 M Na₂SO₄, pH = 6.8) as an electrolyte. EIS was carried out in 5 mM potassium hexacyanoferrate (II and III) and 0.1 M KCl. M-S electrochemical impedance experiments were performed with modified GCE as a working electrode and Pt counter electrode at 6000 Hz in a Na₂SO₄ solution (0.5 M, pH = 6.8). Equation 3 was used to convert the obtained potential against Ag/AgCl/KCl (3M) to a reversible hydrogen electrode (RHE) (normal hydrogen electrode (NHE) at pH = 0).

$$E_{\text{RHE}} = E_{\text{AgCl}} + 0.059\text{pH} + E^{\circ}_{\text{AgCl}} \quad (E^{\circ}_{\text{AgCl}} = 0.197 \text{ V}) \quad (3)$$

2.6. Experimental Design. Nowadays, it has become inevitable to design experiments with suitable software to reduce costs, save time, and attain optimal experiment conditions. For this purpose, experiments were designed with RSM. Design-Expert software (version 12) was used to examine the response of various independent factors. The experimental conditions for the maximum photocatalytic degradation efficiency of IMC by the CCD method were

investigated to study influential factors: pH, amount of mesoporous photocatalyst, IMC concentration, and irradiation time, as well as interactions between parameters. The design consists of five different levels with $\alpha = \pm 2$ (the alpha (α) value can be defined as the calculated distance of each axial point (star point) from the center in the CCD). The pH ranged from 3 to 11, the photocatalyst amount ranged from 5 to 50 mg, the IMC concentration ranged from 10 to 50 mg L⁻¹, and the irradiation time was variable from 5 to 60 min. In this study, three replications were performed to distinguish the significance of error during the experimental run. It should be noted that the experiments were conducted to identify the optimal points during the photodegradation process.

2.7. Adsorption Isotherm Studies. Experimental data in photocatalytic degradation of IMC by the mesoporous NH₂-MCN-2 nanocomposite were investigated with Langmuir, Freundlich, Temkin, and Dubinin–Radushkevich isotherms. To 50 mL IMC aqueous solutions prepared with concentrations of 10, 20, 30, 40, and 50 mg L⁻¹ adjusted at pH = 5, the photocatalyst (0.76 g L⁻¹) was added and stirred at 300 rpm. Next, the concentration of the remaining IMC in the solution was calculated after centrifuging and passing it through a syringe filter with a UV–vis spectrometer using the calibration curve. The equations for Langmuir, Freundlich, Temkin, and Dubinin–Radushkevich isotherms are provided in the Supporting Information (Sections 2.7.1–2.7.4), respectively.

2.8. Investigation of Photocatalytic Degradation Kinetics of IMC. To determine the photocatalytic degradation kinetics of IMC, pseudo-first-order and pseudo-second-order kinetic models, as the two most important models, were investigated. For this purpose, 0.76 g L⁻¹ mesoporous NH₂-MCN-2 nanocomposite was added to 50 mL IMC solutions in concentrations of 10, 20, 30, 40, and 50 mg L⁻¹ at pH = 5. The solutions were stirred at 300 rpm at 25 °C for 10, 20, 46, and 60 min. The samples were centrifuged, and after passing through the syringe filter, the absorption of the solution was recorded with the UV–vis spectrometer. The results showed that the photocatalytic degradation of IMC in all concentrations reached equilibrium after ~46 min. The equations for the pseudo-first-order and pseudo-second-order models are provided in Section 2.8.1 of the Supporting Information.

3. RESULTS AND DISCUSSION

3.1. Characterization of Photocatalysts. X-ray diffraction (XRD) analysis is used to identify the crystalline phase

Table 1. Physical Parameters of g-C₃N₄, NH₂-MIL-88b(Fe), and NH₂-MCN by N₂ Adsorption–Desorption

sample	S_{BET} (m ² /g) ^a	V_p (cm ³ /g) ^b	D (nm) ^c
g-C ₃ N ₄	51.18	0.14	7.30
NH ₂ -MIL-88b (Fe)	142.13	0.45	13.78
NH ₂ -MCN-1	67.04	0.22	14.74
NH ₂ -MCN-2	86.61	0.45	22.85
NH ₂ -MCN-3	76.58	0.56	29.96

^aSpecific surface area. ^bPore volume. ^cPore diameter

present in the material and shows chemical composition information. Figure 1a shows the XRD patterns of g-C₃N₄, NH₂-MIL-88b(Fe), and mesoporous NH₂-MCN nanocomposites with different weight ratios. For g-C₃N₄, the strong peak at $2\theta \sim 27.4^\circ$, which corresponds to the (002) crystal plane,

indicates the accumulation of the aromatic conjugated system.³⁰ The small peak at $2\theta \sim 13^\circ$, corresponding to the (100) crystal plane, is attributed to the stacking of g-C₃N₄ layers.³⁰

The XRD pattern of NH₂-MIL-88b(Fe) shows the main diffraction peaks of its structures at $2\theta \sim 9.25, 10.5, 16.7, 18.9,$ and 21.05 , which is in complete agreement with the reported works.^{31,32} As can be seen from the patterns of NH₂-MCN with different weight ratios, the prominent distinct peaks of NH₂-MIL-88b(Fe) are preserved in the mesoporous nanocomposites. Also, the peak of $2\theta \sim 27.4^\circ$ belonging to g-C₃N₄ has been observed in the XRD patterns. In addition, the specific peak of g-C₃N₄ becomes more evident with an increasing amount of g-C₃N₄ in mesoporous NH₂-MCN nanocomposites.

FT-IR studies were performed to peruse the functional groups and the structures of the mesoporous compounds (Figure 1b). In the spectrum of g-C₃N₄, out-of-plane bending modes of C–N heterocycles appear at 810 cm⁻¹.³³ The absorption bands from 1200 to 1600 cm⁻¹ (1244, 1322, 1414, 1462, and 1573 cm⁻¹) and 1641 cm⁻¹ can be related to C–N aromatic stretching and C=N stretching, respectively.^{33,34} For the NH₂-MIL-88b(Fe) sample, the symmetrical and asymmetrical vibrations of the NH₂ groups are indicated by absorption bands at 3463 and 3340 cm⁻¹.³⁵ Also, the peaks at 1606, 1383, and 1581 cm⁻¹ are attributed to the C=O stretching mode and the carboxyl vibration.^{36,37} The absorption bands at 1255 and 769 cm⁻¹ indicate the C–N stretching and C–H bending vibration of the benzene ring, respectively.^{38,39} In NH₂-MCN, absorption bands at 800 cm⁻¹ corresponding to g-C₃N₄ appear in the mesoporous nanocomposite and become stronger with increasing percentage in the sample, indicating that g-C₃N₄ is successfully incorporated into the structure.

N₂ adsorption–desorption is a valuable method for determining the physical properties of porous material. Data related to the porous texture of the samples are presented in Figure 1c,d, as well as Table 1. The results showed that the adsorption isotherm for all photocatalysts is type IV with the hysteresis loop of type H3.^{35,40} According to the IUPAC classification, the type IV isotherm is related to mesoporous materials. Combining g-C₃N₄ with different weight ratios with MOF causes a decrease in the specific surface area of nanocomposites compared to NH₂-MIL-88b(Fe), indicating that portions of the pores are blocked due to the presence of structural plates of g-C₃N₄.^{41,42} The structural properties of mesoporous g-C₃N₄ (with a size average of approximately 7.30 nm) provide active sites for the improvement of a photocatalytic process.⁴³

Photoluminescence (PL) analysis was used to investigate the rate of recombination of electron–hole pairs produced by radiance. The rate of recombination is linked to the emission peak intensity of the PL spectrum. If emission peaks are generated with high intensity, the material has a speedy recombination rate of electron–hole pair.^{44,45} The PL spectra of C₃N₄, NH₂-MIL-88b(Fe), and mesoporous NH₂-MCN nanocomposites at excitation wavelengths of 333 and 338 nm are presented in Figure 2a. g-C₃N₄ and mesoporous NH₂-MCN-2 nanocomposites have the highest and lowest PL emission intensities, respectively, at a wavelength of ~450 nm. The low separation efficiency of the electron–hole pair in g-C₃N₄ is due to faster recombination.

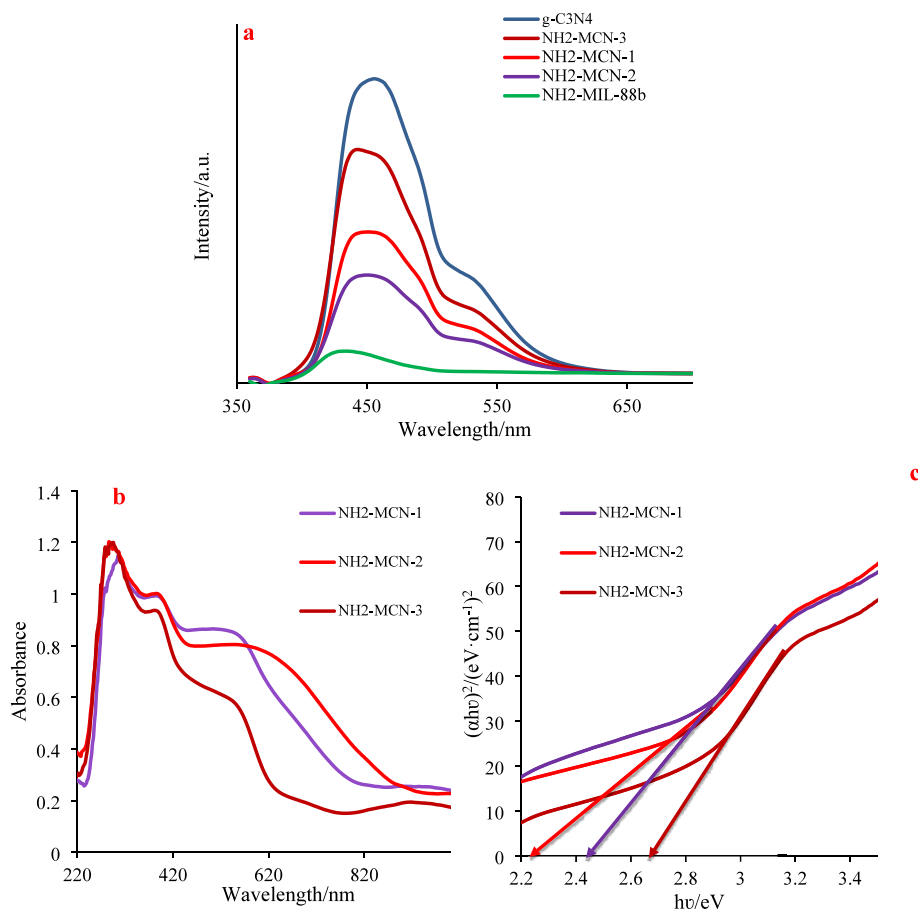


Figure 2. (a) Photoluminescence analysis at the excitation wavelengths of 333 and 338 nm, (b) DRS spectrum, and (c) Kubelka–Munk plots of mesoporous NH₂-MCN nanocomposites with different weight ratios.

The gap energy is one of the critical parameters for photocatalysts. A wide absorption band of mesoporous NH₂-MCN nanocomposites in the range of 220–1000 nm is dominated by an intense absorption band at ~283 nm. In addition to this intense band, there are two weak absorption bands at ~380 and ~588 nm. The peaks observed are related to electron transitions from the highest occupied molecular orbitals (HOMOs) to the lowest unoccupied molecular orbitals (LUMOs), which could be assigned to the existence of the amino group of ligand and Fe₃-μ₃-oxo clusters. It can be said that HOMOs are more of the nature of 2p orbitals of oxygen (organic linkers) and LUMOs are more formed from the participation of metal orbitals.^{46,47} The π–π* transition in the organic linkers can be seen in the absorption in the UV region, while another absorption in the visible region is related to the Fe–O clusters, –NH₂ groups, and g-C₃N₄.⁴⁷

DRS analysis was performed to investigate the amount of energy required for the electron to jump from the valence band to the conduction band (Figure 2b). For mesoporous NH₂-MCN-1, NH₂-MCN-2, and NH₂-MCN-3 nanocomposites, the energy gap was calculated to be ~2.49, 2.29, and 2.69 eV, respectively, using Kubelka–Munk plots (Figure 2c) and eq 4.

$$(\alpha h\nu)^2 = A(h\nu - E_g)^n \quad (4)$$

where α , h , ν , A , and E_g are the absorption coefficient, Planck constant, light frequency, proportionality constant, and energy gap, respectively.

Figure 3 shows the FE-SEM images of g-C₃N₄, NH₂-MIL-88b(Fe), and the mesoporous NH₂-MCN-2 nanocomposite. g-C₃N₄ has a layered structure formed by placing its plates on top of each other (Figure 3a), which is in agreement with previous work.⁴⁸ NH₂-MIL-88b(Fe) has a hexahedral shape with a smooth surface (Figure 3b).⁴⁸ The FE-SEM images of the mesoporous NH₂-MCN-2 nanocomposite showed the presence of both NH₂-MIL-88b(Fe) and g-C₃N₄ in the structure of the nanocomposite (Figure 3c), which indicates that MOF preserves its structure during the synthesis process and has high stability.⁴⁹

The chemical composition and distribution of the elements present in the mesoporous NH₂-MCN-2 nanocomposite were determined by EDX elemental analysis (Figure 4a) and MAP (Figure 4b), so the presence of Fe, O, N, C, and Cl elements was confirmed in its structure.

TEM images of NH₂-MCN-2 (Figure 4c) indicated the close connection of NH₂-MIL-88b(Fe) and g-C₃N₄, which confirmed the formation of the mesoporous nanocomposite. Fe atoms with higher atomic mass cause the formation of a dark area in the images. g-C₃N₄ with C and N elements are also observed in the images as nanosheets.⁴⁷

The TGA curve of the mesoporous NH₂-MCN-2 nanocomposite recorded in a N₂ atmosphere and with a heating rate of 10 °C min⁻¹ showed several stages of weight loss (Figure 5a). The first and second stages happen in the range of 25–400 °C, which is related to the loss of free water molecules, water molecules and solvent (DMF) inside the pores, and the amino group in the MOF.⁵⁰ In the TGA curve, another weight

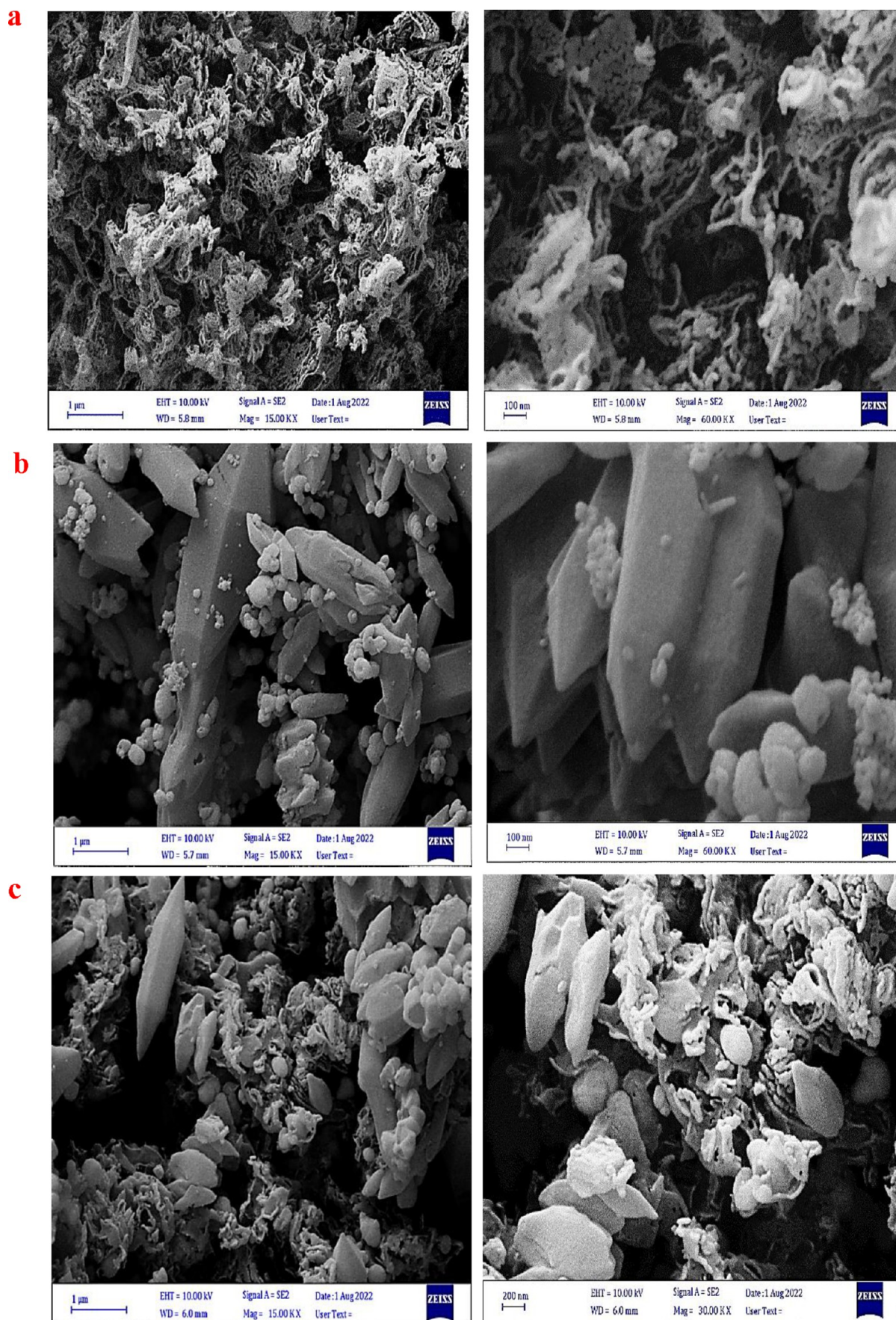


Figure 3. FE-SEM images of (a) $g\text{-C}_3\text{N}_4$, (b) $\text{NH}_2\text{-MIL-88b(Fe)}$, and (c) mesoporous $\text{NH}_2\text{-MCN-2}$ nanocomposite.

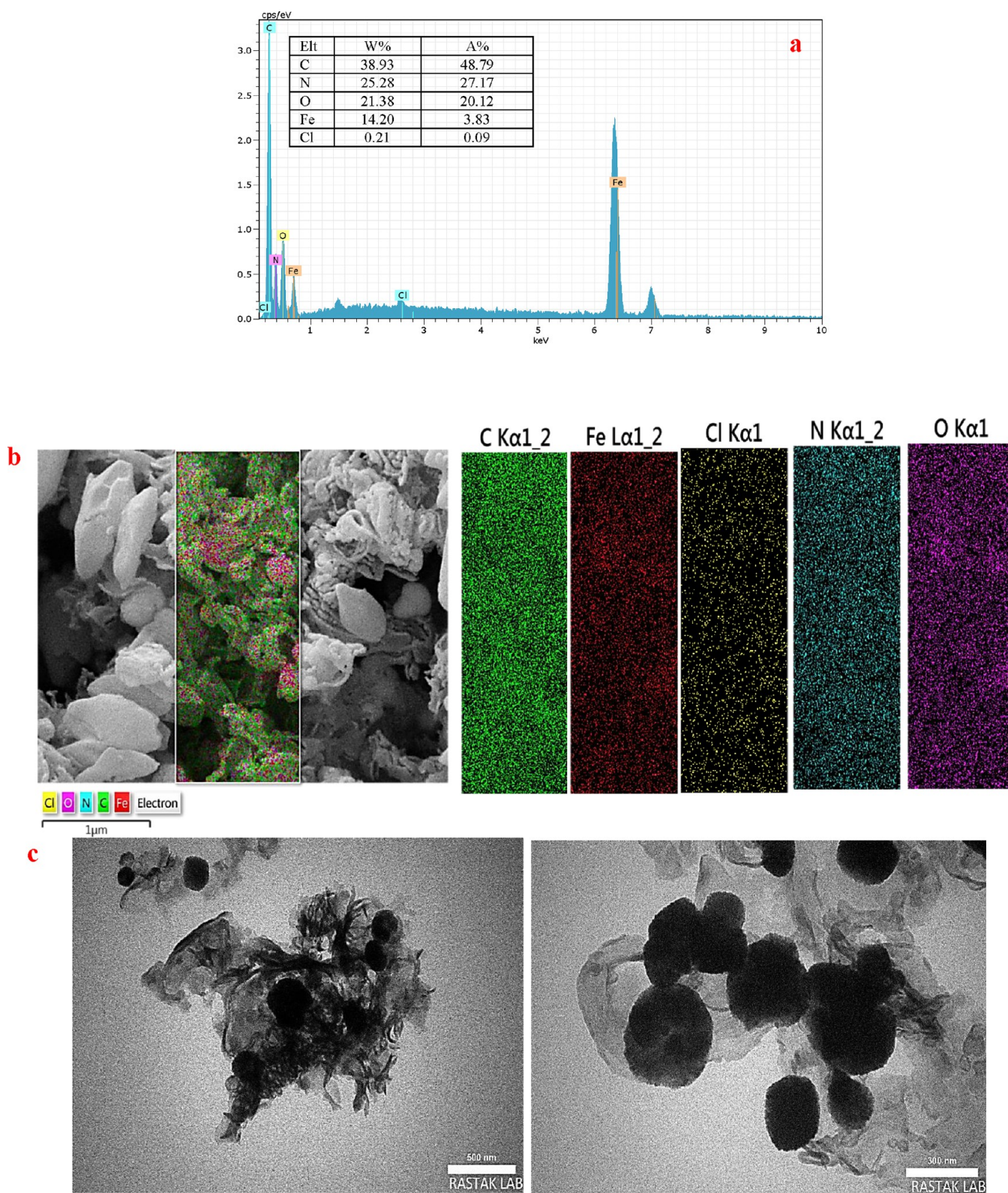


Figure 4. (a) EDX spectrum, (b) MAP, and (c) TEM image of the mesoporous $\text{NH}_2\text{-MCN-2}$ nanocomposite.

loss can be seen at a temperature above $400\text{ }^\circ\text{C}$ related to the decomposition of ligands in $\text{NH}_2\text{-MIL-88b(Fe)}$. Finally, the fourth weight loss in the temperature range of $650\text{--}850\text{ }^\circ\text{C}$ displays the destruction of $\text{g-C}_3\text{N}_4$ species.^{S1}

In AOP, the electric charge on the catalyst surface is considered an influential factor. When $\text{pH} > \text{pH}_{\text{pzc}}$ the

catalyst's surface has a negative charge, while at $\text{pH} < \text{pH}_{\text{pzc}}$ the surface has a positive charge. In this work, the solid addition method and zeta potential were used to measure pH_{pzc} . Determination of pH_{pzc} of $\text{g-C}_3\text{N}_4$, $\text{NH}_2\text{-MIL-88b(Fe)}$, and $\text{NH}_2\text{-MCN-2}$ was performed using a sodium nitrate solution. For this purpose, 0.5 g L^{-1} mesoporous composites

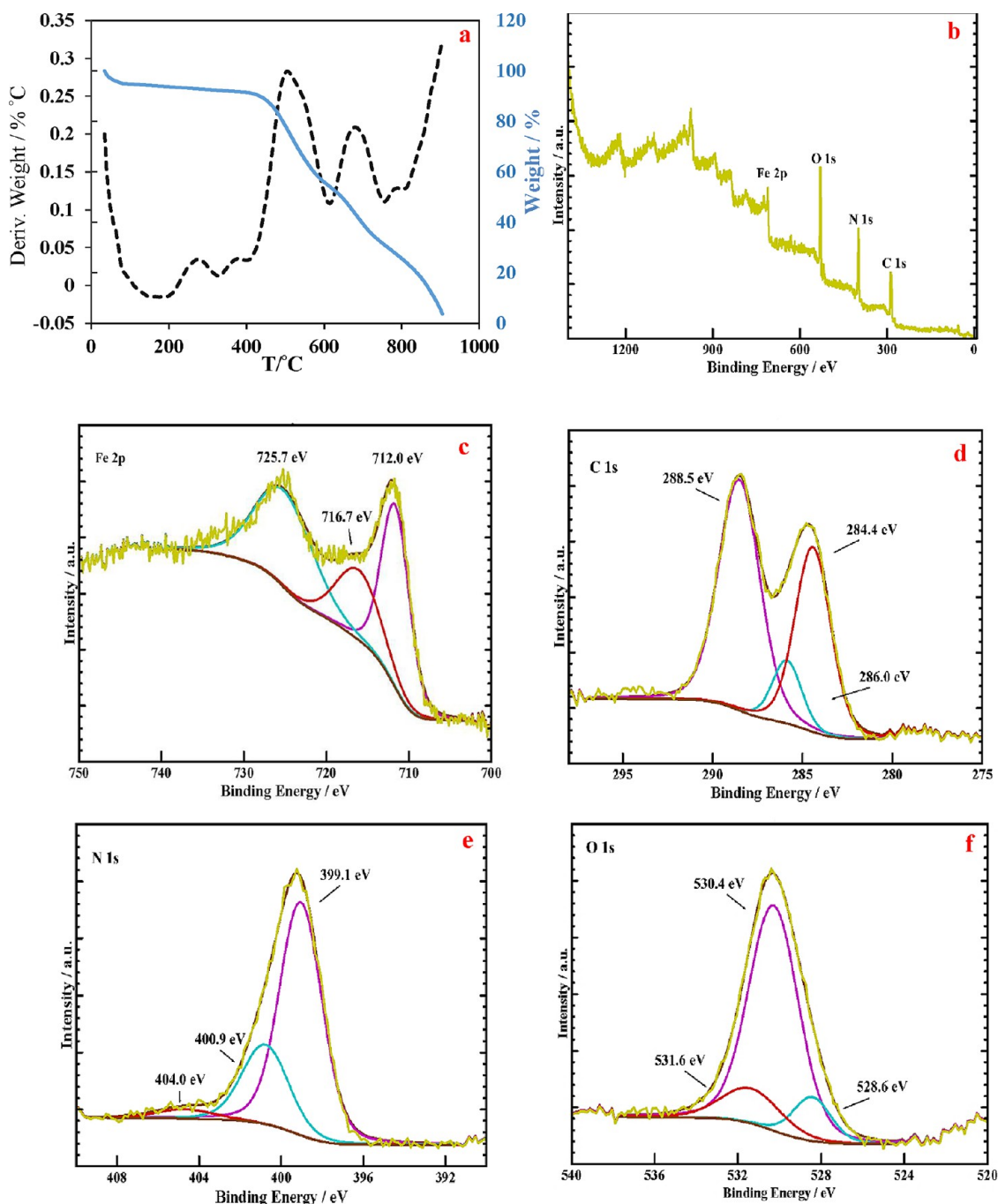


Figure 5. (a) TGA curves and XPS survey spectra of mesoporous $\text{NH}_2\text{-MCN-2}$ nanocomposite and (b) full scans, (c) Fe 2p, (d) C 1s, (e) N 1s, and (f) O 1s.

Table 2. Independent Factors and Their Coded Levels for CCD

factor	unit	low (-1)	middle (0)	high (+1)	$\alpha-$	$\alpha+$
(A) initial concentration of IMC	mg L^{-1}	20	30	40	10	50
(B) pH		5	7	9	3	11
(C) amount of photocatalyst	mg	16.25	27.5	38.75	5	50
(D) irradiation time	min	18.75	32.5	46.75	5	60

were added to 40 mL of sodium nitrate solution (0.1 N) and the pH was adjusted using HCl and NaOH solutions (0.1 M) at pH 2, 4, 6, 9, 12, and 14. The suspension was placed on an incubator shaker (400 rpm) for 24 h at room temperature. Eventually, the pH of each solution was measured and recorded as the final pH.

The results were plotted as ΔpH (final pH – initial pH) vs initial pH in Figure S1a. The pH_{pzc} values for $\text{g-C}_3\text{N}_4$, $\text{NH}_2\text{-MIL-88b(Fe)}$, and mesoporous $\text{NH}_2\text{-MCN-2}$ nanocomposites were obtained as ~ 6.9 , 7.8, and 6.5, respectively. In addition, the variation in zeta potential (-33.3 to 44.7 mV) at different pH values confirmed the results of pH_{pzc} . The plot of zeta potential vs pH_s is shown in Figure S1b.

Table 3. Experiments Performed Based on the Experimental Design and Answers Obtained

run	factor 1 (A)	factor 2 (B)	factor 3 (C)	factor 4 (D)	response (R)
1	0	0	0	2	62.84
2	-1	1	1	1	41.82
3	-1	1	1	-1	29.81
4	0	0	0	0	55.24
5	0	-2	0	0	90
6	2	0	0	0	38.87
7	0	0	0	0	54.26
8	1	1	1	1	34.39
9	1	1	-1	1	30.15
10	1	-1	-1	-1	46.94
11	0	0	-2	0	28.96
12	1	-1	1	1	75.97
13	-1	-1	-1	1	85.28
14	1	-1	1	-1	50.24
15	0	0	2	0	63.11
16	1	-1	-1	1	69.93
17	-1	-1	-1	-1	55.89
18	1	1	-1	-1	20.48
19	0	2	0	0	25.36
20	-1	1	-1	1	36.34
21	0	0	0	0	50.26
22	0	0	0	0	56.27
23	0	0	0	0	58.01
24	0	0	0	0	52.22
25	-2	0	0	0	64.01
26	1	1	1	-1	27.36
27	0	0	0	-2	18.02
28	-1	1	-1	-1	23.36
29	-1	-1	1	-1	67.95
30	-1	-1	1	1	94.85

In the XPS spectrum of NH₂-MCN-2, signals of Fe, C, N, and O were observed, which offers the successful synthesis of the mesoporous nanocomposite (Figure 5b). The peaks of Fe 2p spectra with high resolution are presented in Figure 5c.

Three peaks at 712.0, 725.7, and 716.7 eV are attributed to Fe 2p_{3/2}, Fe 2p_{1/2}, and their satellite, respectively, which display the presence of Fe(III).^{47,52} The C 1s spectrum indicates three peaks centered at 284.4, 286.0, and 288.5 eV (Figure 5d). The 284.8 eV peak was considered as the calibration reference. The peak in the 284.4 eV region corresponds to the alkyl carbon components in the benzene ring, C–H, and C–C bonds. The peaks at 286 and 288.5 eV are related to the area C–N–C group in g-C₃N₄ and the carboxylate functional group (O–C=O) of H₂BDC-NH₂ or the sp² carbon in the thiazine ring (N–C=N), respectively.^{47,53} The N 1s spectrum of the mesoporous NH₂-MCN nanocomposite provides three peaks at 399.1, 400.9, and 404.0 eV, which are matched to the CN=C of sp²-bonded aromatic, N–(C)₃ of tertiary N, and C–N–H groups from g-C₃N₄, respectively (Figure 5e).^{47,54} Eventually, the O 1s spectrum demonstrates three peaks at around 528.6, 530.4, and 531.6 eV, which are ascribed to the oxygen components of terephthalate linkers, Fe–O bonds in the ligand, and possibly H₂O absorption on the surface of the catalyst, respectively (Figure 5f).^{21,47,55}

3.2. Degradation of IMC. In this part, the photocatalytic degradation rate of IMC was investigated with mesoporous NH₂-MCN nanocomposites with various weight ratios of g-C₃N₄. Specific amounts of each photocatalyst (0.3 g L⁻¹) were added separately to 50 mL IMC solutions with a specific concentration (30 mg L⁻¹) under the same experimental conditions (pH = 3 and ambient temperature). The solutions were stirred at 300 rpm for 15 min without light, and sampling was done at specified time intervals. After centrifuging and passing the solutions through a syringe filter (0.45 μm), the IMC residue in the solution was investigated by a two-beam UV–vis spectrophotometer. Next, the solutions were exposed to the visible light of a halogen lamp (λ > 400 nm with a power of 300 W) for 60 min, sampling was done at specified time intervals, and the IMC concentration was determined. The photodegradation rates for NH₂-MCN-1, NH₂-MCN-2, and NH₂-MCN-3 were obtained at 75.00, 92.05, and 55.04%, respectively (Figure S2). It was observed that for each photocatalyst, degradation increases with increasing time.

Table 4. ANOVA for Optimization of Photocatalytic Degradation of IMC

source	sum of squares	df	mean square	F-value	p-value	significant
model	12,299.46	14	878.53	49.08	<0.0001	significant
A-A	705.47	1	705.47	39.41	<0.0001	
B-B	7798.34	1	7798.34	435.67	<0.0001	
C-C	623.42	1	623.42	34.83	<0.0001	
D-D	2327.36	1	2327.36	130.02	<0.0001	
AB	109.94	1	109.94	6.14	0.0256	
AC	10.73	1	10.73	0.5992	0.4509	
AD	15.72	1	15.72	0.8783	0.3635	
BC	3.92	1	3.92	0.2190	0.6465	
BD	250.59	1	250.59	14.00	0.0020	
CD	0.7056	1	0.7056	0.0394	0.8453	
A ²	11.46	1	11.46	0.6404	0.4361	
B ²	22.89	1	22.89	1.28	0.2759	
C ²	109.46	1	109.46	6.12	0.0258	
D ²	316.88	1	316.88	17.70	0.0008	
residual	268.49	15	17.90			
lack of fit	229.35	10	22.94	2.93	0.1235	not significant
pure error	39.14	5	7.83			
cor total	12567.96	29				

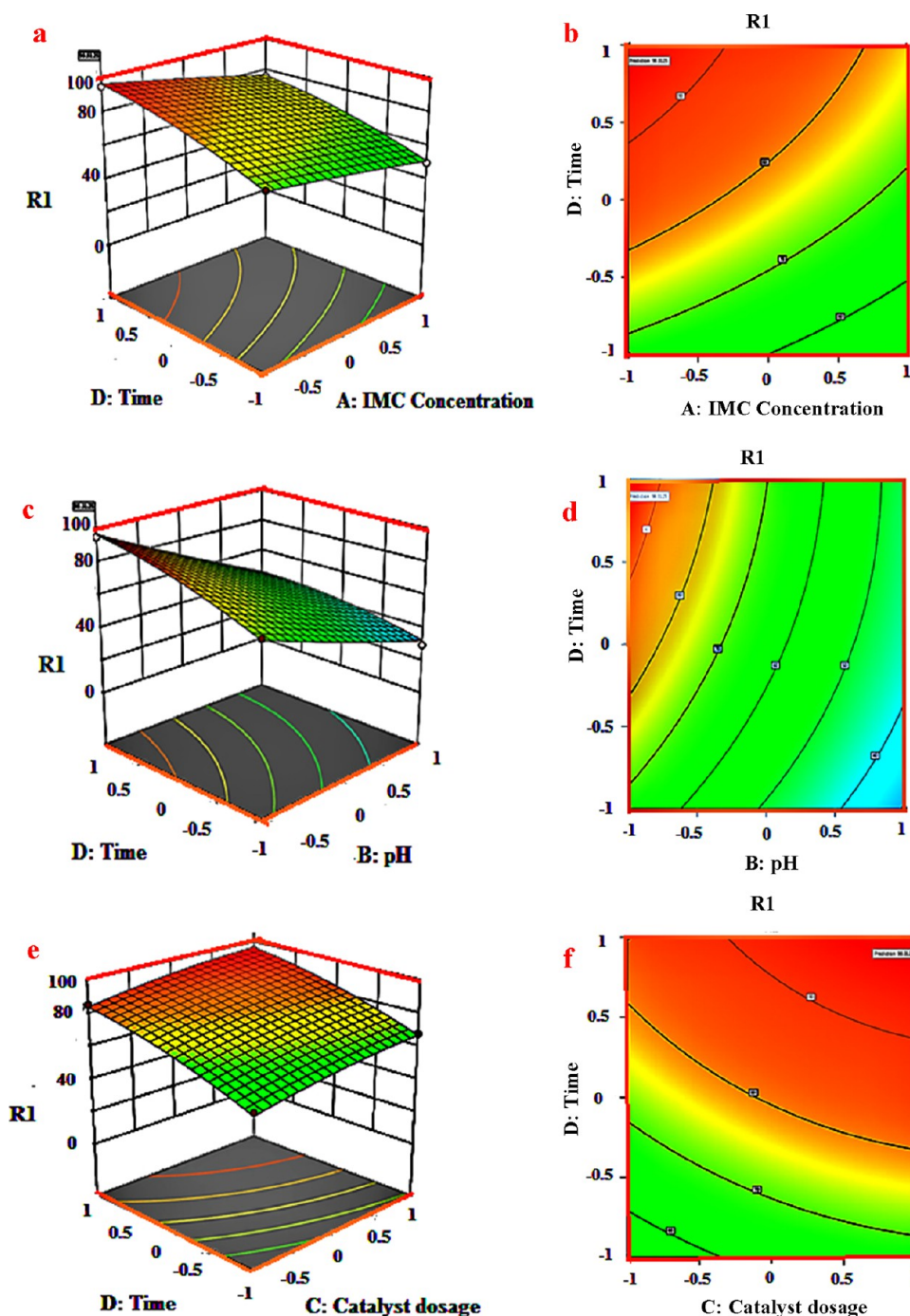


Figure 6. 3D surface plots and 2D contour for the interactions of (a, b) initial concentration and degradation time, (c, d) pH and degradation time, and (e, f) amount of photocatalyst and degradation time.

The mesoporous $\text{NH}_2\text{-MCN-2}$ nanocomposite has higher photocatalyst efficiency in the IMC degradation process than other mesoporous nanocomposites because it has a lower energy gap and higher surface area. In the mesoporous $\text{NH}_2\text{-MCN-2}$ nanocomposite, a low rate of hole–electron recombination caused the degradation of IMC with higher efficiency. Figure S3a–c shows the morphology, EDX elemental analysis, and MAP analysis of mesoporous $\text{NH}_2\text{-MCN-2}$ nanocomposites, respectively, which defined the high structural stability of photocatalysts during the process (1st).

3.3. Designing Experiment in Photocatalytic Degradation of IMC. 3.3.1. Investigating the Photocatalytic

Process Based on CCD and RSM. The RSM method was used to optimize the photocatalytic degradation of IMC using four factors. The total number of experiments was 30 runs using five CCD levels with three repetitions. A, B, C, and D are the coded values of IMC initial concentration, pH, amount of photocatalyst, and irradiation time, respectively, presented in Table 2. The experimental results of IMC photocatalytic degradation (%) were predicted based on the designed initial conditions, and they are shown in Table 3 and eq 5.

$$R = 54.38 - 3.71A - 15.12B + 5.61C + 13.47D + 2.62AB - 3.96BD - 2.00C^2 - 3.40D^2 \quad (5)$$

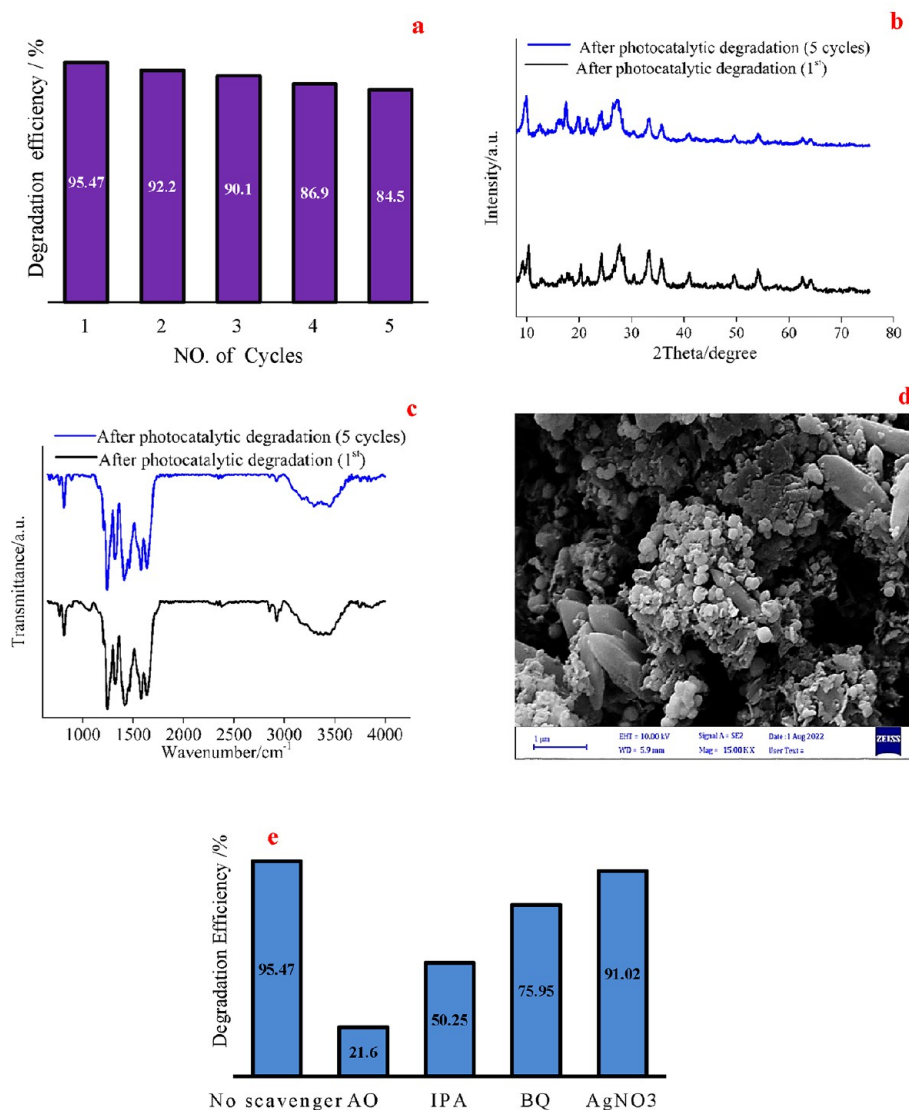


Figure 7. (a) Reusability of the mesoporous NH₂-MCN-2 nanocomposite in optimal experiment conditions (initial concentration of 20 mg L⁻¹ IMC, amount of photocatalyst of 0.76 g L⁻¹, pH = 5, and degradation time ~46 min), (b) XRD patterns, (c) FT-IR and (d) FE-SEM image of photocatalytic degradation of IMC after five cycles, and (e) photocatalytic degradation in the presence of trapping agents (2 mmol).

Based on the values of the coefficients in the regression model, the order in which the variables affect the photocatalytic degradation of IMC is pH (B) > irradiation time (D) > initial concentration of IMC (A) > amount of photocatalyst (C). The significance and adequacy of the proposed model were perused by ANOVA. The results presented excellent agreement between the predicted and experimental values of photocatalytic degradation of IMC. The model is statistically significant with linear terms, interactions, and quadratic terms. The effectiveness and significance of the proposed model were gained with the *F*-value, *p*-value, related *R*², predicted *R*², and adjusted *R*², which are given in Table 4 and Table S1.

The *p*-value and *F*-value of the model for the photocatalytic degradation of IMC were obtained as <0.0001 and 49.08, respectively, which means that the model is significant. All independent variables such as A, B, C, D, BD, AB, C², and D², which have *p* < 0.05, indicate the significance of the term in the model. The *R*²-predicted value shows good agreement with the *R*² and *R*²-adjusted values. The *F*-value of the lack of fit (LOF) is obtained as 2.93, which is insignificant because the *p*-value is

0.1235. Figure S4 shows good agreement between the predicted and actual values, indicating the adequacy and significance of the mode.

3.3.2. Effect of Factors in the Photocatalytic Process. Three-dimensional (3D) response surface and two-dimensional contour (2D) plots were utilized to peruse the effects of the experiment variables and their interaction on the photocatalytic degradation of IMC. Since the time factor has a direct relationship with process efficiency, the impact of each factor has been studied along with the time factor (Figure 6a–f).

3.3.2.1. Effect of Initial Concentration of IMC. Figure 6a,b shows that the photocatalytic degradation efficiency of IMC decreases with increasing concentration. It can be attributed to the following reasons: (a) The increase in IMC concentration leads to the intensification of dispersion in the solution and turbidity, which reduces the penetration of radiance into the solution, as well as photon absorption by the photocatalyst. (b) At high IMC concentrations, the formation of oxidizing species is reduced through the coverage of active sites by IMC

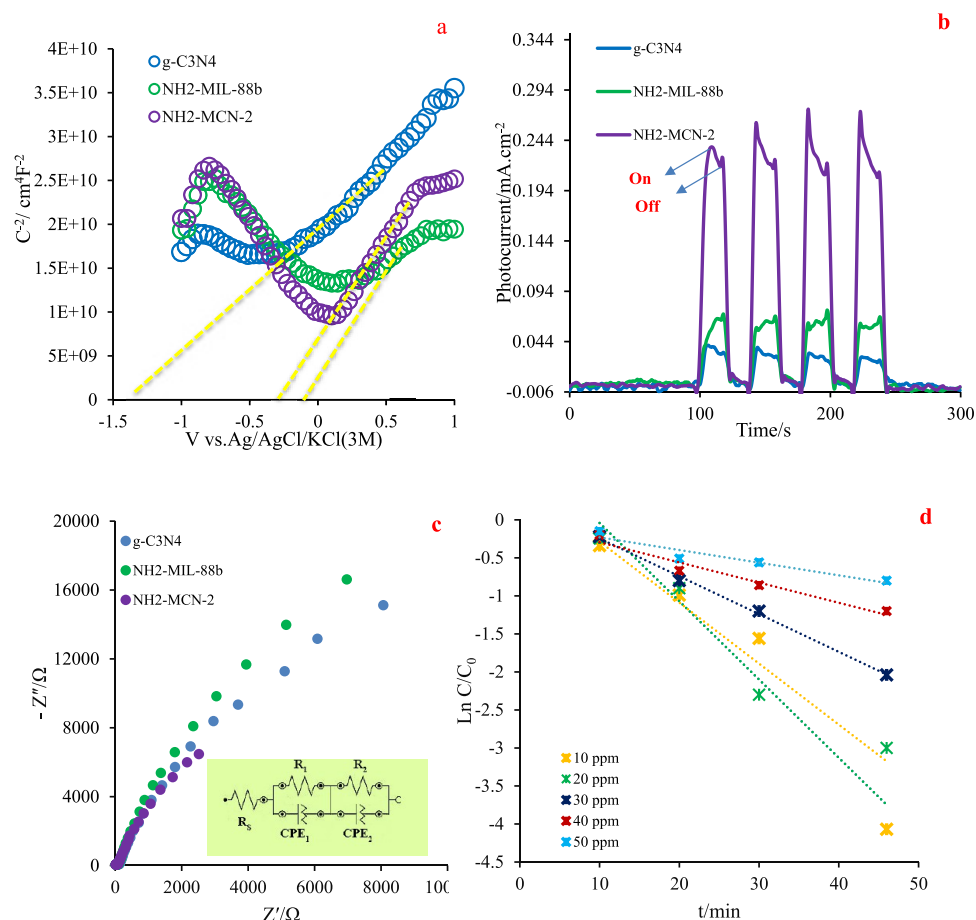


Figure 8. (a) Mott–Schottky plots at a frequency of 6000 Hz, (b) photocurrent response and (c) Nyquist plots of g-C₃N₄, NH₂-MIL-88b(Fe), and mesoporous NH₂-MCN-2 nanocomposite, and (d) kinetic plot of pseudo-first-order model in photocatalytic degradation of IMC by NH₂-MCN-2.

Table 5. Isotherm Parameters for Photocatalytic Degradation of IMC by the Mesoporous NH₂-MCN-2 Nanocomposite

isotherm	parameter	result
Langmuir	q_m (mg g ⁻¹)	35.7142
	K_L (L mg ⁻¹)	0.1351
	R_L (20 mg L ⁻¹)	0.2702
	R^2	0.9913
	Freundlich	K_F (L mg ⁻¹)
$1/n$		1.9296
R^2		0.9360
Temkin	B	8.3180
	K_T (L g ⁻¹)	1.1297
	b_T (J mol ⁻¹)	297.8566
	R^2	0.9681
Dubinin–Radushkevich	q_m (mg g ⁻¹)	25.2796
	K_{DR} (mol ² kJ ⁻²)	2×10^{-6}
	E (kJ mol ⁻¹)	2
	R^2	0.9405

molecules or the absorption of photons by them. Consequently, a finite number of oxidizing species can degrade IMC molecules.

3.3.2.2. Effect of pH. One of the influential factors in the photocatalytic degradation of pollutants is solution pH, which affects the surface charge of the catalyst and its structure.⁵⁶ In

Table 6. Comparison of Different Photocatalytic Performances for IMC Degradation

photocatalyst	photocatalytic degradation efficiency of IMC (%)	reference
Au@PPy-C/SnO ₂	93.18	57
Bi _{12.7} Co _{0.3} O _{19.35}	96	58
g-C ₃ N ₄ /TiO ₂	93	59
g-C ₃ N ₄ /ZnO (20:80)	56	60
TiO ₂	90	61
Bi ₂ Co ₂ C ₄₂ H ₃₆ N ₆ O ₃₃	81	62
PANI/ZnO-CoMoO ₄	97	63
SO ₄ /Ag ₃ PO ₄	75	64
PANI/WO ₃ -CdS	94	65
Ag/AgBr	90	66
GO@TiO ₂	93	67
GO/Fe ₃ O ₄ /TiO ₂ -NiO	97.47	68
ZnO/CoFe ₂ O ₄	98.1	69
TiO ₂	90.24	70
U-g-C ₃ N ₄ (from urea)	90	71
M-g-C ₃ N ₄ (from melamine)	42.9	71
NH ₂ -MCN-2	95.47	this study

this study, the kinetics of photocatalytic degradation of IMC was studied in the range of pH from 3 to 11, and the results show high degradation efficiency in acidic media (Figure 6c,d). At lower pH values of solution, the mesoporous NH₂-MCN-2

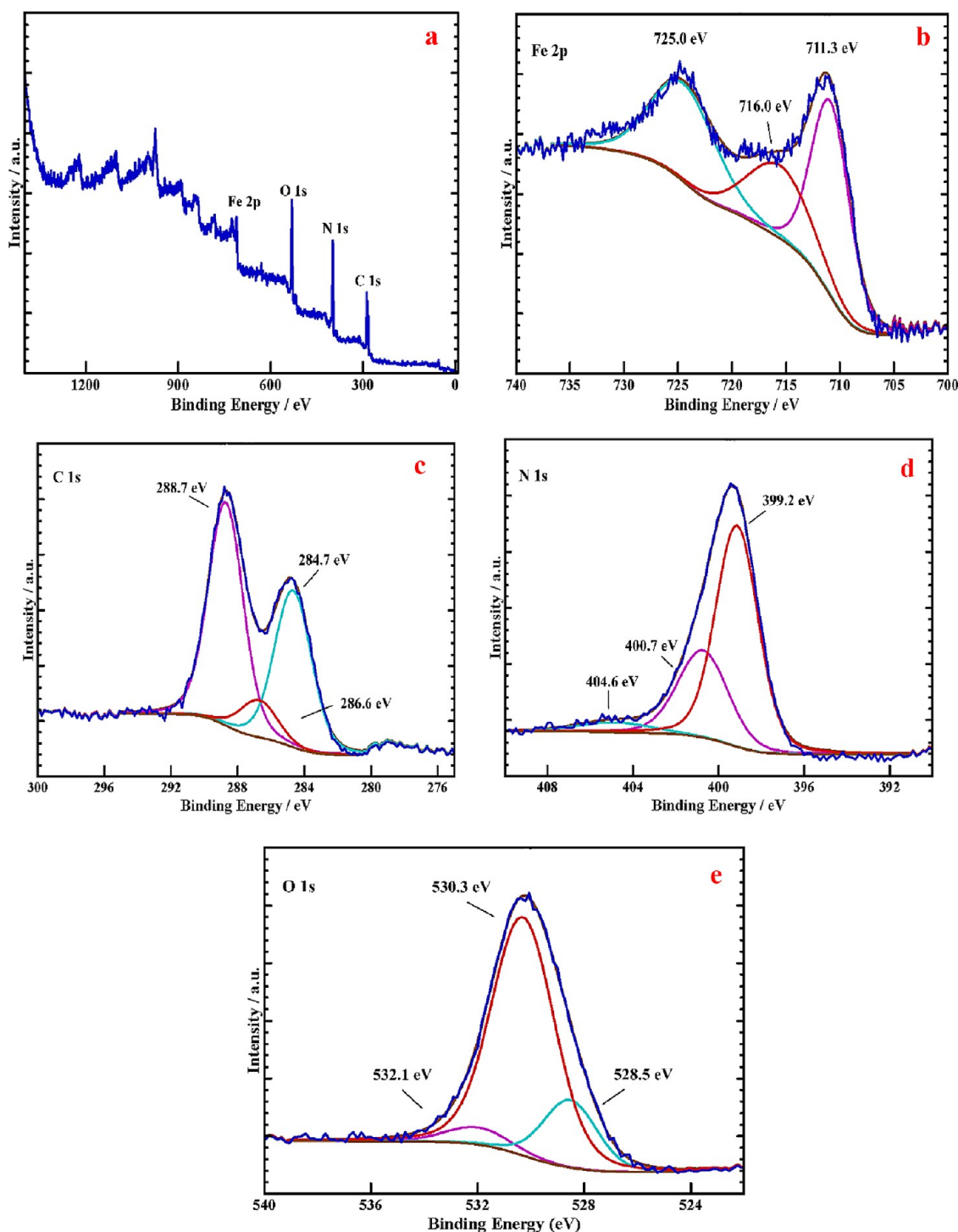


Figure 9. XPS survey spectra of the mesoporous $\text{NH}_2\text{-MCN-2}$ nanocomposite: (a) full scan, (b) Fe 2p, (c) C 1s, (d) N 1s, and (e) O 1s after photocatalytic degradation of IMC.

nanocomposite with $\text{pH}_{\text{pzc}} \sim 6.5$ has a positive charge. In an acidic environment, IMC with $\text{pK}_a = 11$ cannot release H^+ ions to the reaction solution. Due to the presence of electron-rich aromatic rings in the IMC molecule, it probably adsorbed on the positively charged surface of the photocatalyst. In addition to electrostatic/acid–base/ π – π interactions, hydrogen bonding may affect the photocatalytic degradation efficiency in aqueous solutions.¹³

3.3.2.3. Effect of Photocatalyst Amount. The relevance between the photocatalytic degradation efficiency of IMC and

the amount of photocatalyst is shown in Figure 6e,f. Increasing the amount of mesoporous $\text{NH}_2\text{-MCN-2}$ nanocomposite leads to an increment in active sites and, therefore, the adsorption of IMC molecules on its surface. In addition, by increasing the amount of photocatalyst, the number of photons absorbed increases, and as a result, by increasing the production of electron–hole pairs, conditions are provided for more photodegradation.

3.4.3. Determining the Optimum Condition of Factors. After investigating the effect of the main factors and their

interaction in photocatalytic degradation of IMC, to save time, cost, and high efficiency, certain levels of effective factors were selected to determine the maximum degradation capacity of the mesoporous NH₂-MCN-2 nanocomposite (Figure S5). According to the results, the optimal points were obtained in the IMC initial concentration of 20 mg L⁻¹, the amount of photocatalyst of 0.76 g L⁻¹, pH 5, and the irradiation time of 46' 25". Also, the predicted value (96.31%) agrees with the actual values of the maximum degradation of IMC (95.47%).

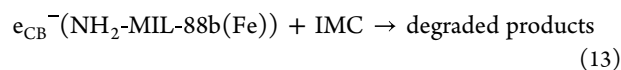
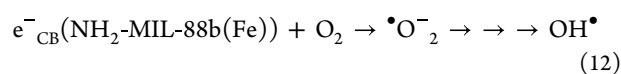
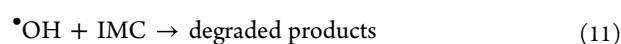
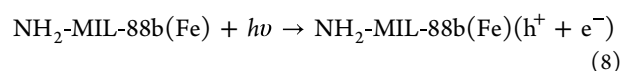
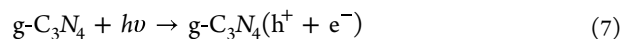
3.4. Stability and Reusability. One of the characteristics of a functional photocatalyst is its stability and reusability. For this purpose, the mesoporous NH₂-MCN-2 nanocomposite was used in the photocatalytic degradation of IMC. After the end of each cycle, the photocatalyst was separated using a centrifuge, washed with ethanol, and then dried at 60 °C for 12 h in a vacuum oven. The results in Figure 7a show that the mesoporous NH₂-MCN-2 nanocomposite has strong reusability performance after five cycles. Figure 7b indicates that the XRD patterns of the mesoporous NH₂-MCN-2 nanocomposite before and after the reaction are similar. In addition, the FT-IR spectra of the materials confirm that there is no significant change in the structural properties of the photocatalyst (Figure 7c). FE-SEM of the mesoporous NH₂-MCN-2 nanocomposite (Figure 7d) shows that the morphology of the mesoporous NH₂-MCN-2 nanocomposite remains unchanged after the photocatalytic reaction. For more investigation, EDX and MAP analyses of the sample were performed, and the results confirm that significant components of the catalyst including NH₂-MIL-88b(Fe) and g-C₃N₄ can be found after recycling experiment (Figure S6a,b). After five cycles, the efficiency of photocatalytic degradation of IMC decreases from 95.47 to 84.5%. This reduction may be the absorption of resistant intermediate products on the surface of the photocatalyst and those occupying the active sites, resulting in the absorption of less light and the production of charge carriers on the surface of the photocatalyst, followed by less degradation of IMC.

3.5. Effects of Trapping Agents. To peruse the main active species in photocatalytic degradation of IMC by the mesoporous NH₂-MCN-2 nanocomposite, BQ (O²⁻), IPA (•OH), AO (h⁺), and AgNO₃ (e⁻) species were added as trapping agents with a concentration of 2 mmol to the aqueous solution containing IMC. The results show that when AgNO₃ and BQ species are added to the IMC solution, they have a negligible effect on the degradation (Figure 7e). The photocatalytic degradation of IMC by the mesoporous NH₂-MCN-2 nanocomposite is clearly decreased by the addition of AO. In addition, the results exhibited that the degradation decreases with the addition of IPA. Therefore, it is proved that h⁺ is the main active species in the reaction, and •OH is the auxiliary active species.

3.6. Mechanism of Photocatalytic Degradation. To determine the flat band potential (V_{FB}) of mesoporous composites, an M-S plot is recorded at a frequency of 6000 Hz (Figure 8a). g-C₃N₄ has higher negative V_{FB} of ~-1.4 V vs Ag/AgCl/KCl (3M) compared to NH₂-MIL-88b(Fe), and mesoporous NH₂-MCN-2 nanocomposites have E_{FB} of ~-0.3 and ~-0.21 V, respectively. The CB band positions of g-C₃N₄, NH₂-MIL-88b(Fe), and mesoporous NH₂-MCN-2 nanocomposites have been obtained as -1.20, -0.10, and -0.01 V vs NHE, respectively.⁴⁷ Moreover, the values of the energy gap were calculated by using DRS analysis. Next, using the following equation, E_{VB} was obtained.

$$E_{CB} = E_{VB} - E_g \quad (6)$$

The E_{VB} values of g-C₃N₄, NH₂-MIL-88b(Fe), and the mesoporous NH₂-MCN-2 nanocomposite were estimated as 1.56, 1.58, and 2.27 V vs NHE, respectively. A positive slope at the M-S plot displays an n-type semiconductor. Irradiation of visible light to the mesoporous NH₂-MCN-2 nanocomposite causes the production of charge carriers (electron-hole pair) by NH₂-MIL-88b(Fe) and g-C₃N₄; thus, the photogenerated holes in the VB of g-C₃N₄ and the photogenerated electrons in the CB of NH₂-MIL-88b(Fe) increase the separation efficiency of photocarriers and finally cause the improvement of the photocatalytic performance (eqs 7–13).



3.7. Electrochemical and Photoelectrochemical Investigations. The photocurrent response and EIS of g-C₃N₄, NH₂-MIL-88b(Fe), and mesoporous NH₂-MCN-2 nanocomposites were recorded to investigate the effect of charge transfer and separation of generated charge carriers (electron-hole pair). Figure 8b shows the photocurrent-time response of different photocatalysts with four on-off cycles. Compared to g-C₃N₄ and NH₂-MIL-88b(Fe), the photocurrent response of the mesoporous NH₂-MCN-2 nanocomposite is significantly increased, which proves that g-C₃N₄ and NH₂-MIL-88b(Fe) help to separate the charges produced in the photodegradation process. EIS studies express the difficulty of charge transfer on the catalyst surface. In the Nyquist plot, the mesoporous NH₂-MCN-2 nanocomposite has the most minor diameter of the semicircle, which indicates less charge transfer resistance and a fast electron transfer rate in the electrode-electrolyte interface (Figure 8c).

3.8. Kinetic Studies. One of the critical factors in the process of adsorption is to examine and study its kinetics. The most critical isotherm models including first- and second-order pseudo models were investigated. The photocatalytic degradation of IMC as a change of Ln C/C₀ vs irradiation time (t) follows a straight line with a high correlation coefficient (R²) (Figure 8d). The results illustrated that the photocatalytic degradation of IMC follows first-order kinetics. The rate constant (k) obtained in the conditions of catalyst amount = 0.76 g L⁻¹, different initial concentrations of IMC (10–50 mg L⁻¹), pH = 5, and irradiation time ~46 min is equal to 0.08 min⁻¹ (Table S2).

3.9. Adsorption Isotherm. The adsorption behavior of IMC on the surface of the mesoporous NH₂-MCN-2 nanocomposite was investigated by Langmuir, Freundlich, Temkin, and Dubinin-Radushkevich models (Figure S7a–d). The obtained coefficients (R²) show that the adsorption

process agrees better with the Langmuir model. The parameters of the isotherm models for adsorption are presented in Table 5. The photocatalytic performance for the decomposition of IMC was compared with other photocatalysts in Table 6.

3.10. Investigation of Photocatalytic Degradation of IMC. Comparing the results of XPS analysis on the surface of the mesoporous NH₂-MCN-2 nanocomposite before and after the photodegradation process shows good agreement (Figure 9a–e). All peaks have almost the same bonding energy, and no significant change has occurred in their position. Therefore, it can be said that there are no physicochemical interactions between IMC and NH₂-MCN-2.

The HPLC method was also used to investigate the photodegradation process. Two solutions of IMC (50 mL) were prepared under the optimal experiment conditions. One of the solutions was kept as a stock solution, and the mesoporous NH₂-MCN-2 nanocomposite was added to the other solution in the dark. Next, the solution was exposed to visible light. After the necessary time (~46 min) in the photodegradation process of IMC, the catalyst was filtered, and the solution was injected into the HPLC instrument with a detector adjusted at the wavelength of 270 nm. The results shown are consistent with the UV–vis results reported in this work and confirm the photodegradation of IMC (Figure S8).

4. CONCLUSIONS

In this work, mesoporous NH₂-MCN nanocomposites with different weight ratios of g-C₃N₄ (CN = 125, 250, and 500 mg) were synthesized by the solvothermal method and used for photocatalytic purposes. Among them, the mesoporous NH₂-MCN-2 nanocomposite was proposed as a promising candidate for photodegradation of IMC due to its lower energy gap (~2.29 eV) and higher specific surface area (86.61 m² g⁻¹). In the following, the CCD method was used to investigate four influential factors in the photocatalytic degradation of IMC from aqueous solutions. RSM was used to optimize the photodegradation process. The optimal points were obtained as follows: initial concentration of 20 mg L⁻¹ IMC, amount of photocatalyst of 0.76 g L⁻¹, pH 5, and degradation time of ~46 min. The photocatalytic degradation of 95.47% for IMC was achieved after irradiation by NH₂-MCN-2. The agreement between the parameters and the response of the model based on the results of ANOVA shows the validity of the model. NH₂-MCN-2 showed high stability and reusability. According to the coefficient of determination (*R*²) obtained from the kinetic and isotherm models, the photodegradation process is controlled using the pseudo-first-order model (*k* = 0.08 min⁻¹), and the isotherm data were more compatible with the Langmuir model. The EIS results as well as the photocurrent response of NH₂-MCN-2 showed a significant improvement compared to g-C₃N₄ and NH₂-MIL-88b(Fe) according to electron transfer rate and photocatalytic activity. The reason is due to the synergistic effect between g-C₃N₄ and NH₂-MIL-88b(Fe). The *E*_{CB} band positions of the g-C₃N₄ and NH₂-MIL-88b(Fe) photocatalysts as well as the *E*_{VB} band vs NHE were obtained using M-S electrochemical impedance at -1.20, -0.10, 1.56, and 1.58 V, respectively. The results achieved from trapping experiments identified the role of the effective active species of h⁺ and •OH for the photocatalytic degradation of IMC.

■ ASSOCIATED CONTENT

Supporting Information

The Supporting Information is available free of charge at <https://pubs.acs.org/doi/10.1021/acsomega.3c10281>.

Determination of pH_{pzc} and zeta potentials (Figure S1); photocatalytic degradation of IMC by mesoporous NH₂-MCN nanocomposites (Figure S2); FE-SEM, EDX elemental, and MAP analyses of the mesoporous NH₂-MCN-2 nanocomposite after photocatalytic degradation of IMC (1st) (Figure S3); statistical parameters related to the proposed model of photocatalytic degradation of IMC (Table S1); normal probability plot of residuals, standard plots of residuals vs predicted and residuals vs run number, and plot of predicted vs actual values (Figure S4); suggested points (optimum points) of model in photocatalytic degradation of IMC (Figure S5); EDX and elemental mapping analyses of the NH₂-MCN-2 photocatalyst after five cycles of IMC degradation (Figure S6); pseudo-first-order kinetic parameters in photocatalytic degradation of IMC (Table S2); isotherm plots of IMC adsorption on the surface of the mesoporous NH₂-MCN-2 nanocomposite (Figure S7); chromatograms of IMC solution before and after photocatalytic degradation (Figure S8) (PDF)

■ AUTHOR INFORMATION

Corresponding Author

Shahram Ghasemi – Faculty of Chemistry, University of Mazandaran, Babolsar 4741695447, Iran; orcid.org/0000-0002-7988-7809; Phone: +981135302388; Email: sghasemi@umz.ac.ir

Authors

Elham Chiani – Department of Analytical Chemistry, Faculty of Chemistry, University of Mazandaran, Babolsar 47416-95447, Iran

Seyed Naser Azizi – Department of Analytical Chemistry, Faculty of Chemistry, University of Mazandaran, Babolsar 47416-95447, Iran

Complete contact information is available at:

<https://pubs.acs.org/doi/10.1021/acsomega.3c10281>

Notes

The authors declare no competing financial interest.

■ ACKNOWLEDGMENTS

The authors acknowledge the scientific and technical supports of University of Mazandaran, Iran for this research work.

■ REFERENCES

- Arnaud, C. H. Microparticles protect bees from pesticides. *C&EN* **2021**, 99 (20), 11.
- Zhang, B.; Li, B.; Wang, Z. Creation of Carbazole-Based Fluorescent Porous Polymers for Recognition and Detection of Various Pesticides in Water. *ACS Sensors* **2020**, 5 (1), 162–170.
- Meng, Z.; Liu, L.; Yan, S.; Sun, W.; Jia, M.; Tian, S.; Huang, S.; Zhou, Z.; Zhu, W. Gut microbiota: a key factor in the host health effects induced by pesticide exposure. *J. Agric. Food Chem.* **2020**, 68, 10517–10531.
- Wise, C. F.; Hammel, S. C.; Herkert, N. J.; Ospina, M.; Calafat, A. M.; Breen, M.; Stapleton, H. M. Comparative Assessment of Pesticide Exposures in Domestic Dogs and Their Owners Using

Silicone Passive Samplers and Biomonitoring. *Environ. Sci. Technol.* **2022**, *56* (2), 1149–1161.

(5) Li, W.; Wang, L.; Shi, P.; Gao, Z. Determination and Correlation of Solubility of Forms I and II of Imidacloprid in Seven Pure Solvents from 293.15 to 333.15 K. *Journal of Chemical & Engineering Data* **2020**, *65*, 5421–5427.

(6) Loganathan, B. G.; Ahuja, S.; Subedi, B. (2020). Synthetic Organic Chemical Pollutants in Water: Origin, Distribution, and Implications for Human Exposure and Health, *Contaminants in Our Water: Identification and Remediation Methods, Chapter 2*, 13–39.

(7) Zhen, Y.; Ge, L.; Chen, Q.; Xu, J.; Duan, Z.; Looor, J. J.; Wang, M. Latent Benefits and Toxicity Risks Transmission Chain of High Dietary Copper along the Livestock–Environment–Plant–Human Health Axis and Microbial Homeostasis: A Review. *J. Agric. Food Chem.* **2022**, *70*, 6943–6962.

(8) Sharma, T.; Kaur, M.; Sobti, A.; Rajor, A.; Toor, A. P. Sequential micro-bial-photocatalytic degradation of imidacloprid. *Environ. Eng. Res.* **2020**, *25*, 597–604.

(9) Liu, G. Y.; Li, L. Y.; Xu, D. H.; et al. Metal-organic framework preparation using magnetic graphene oxide-beta-cyclodextrin for neonicotinoid pesticide adsorption and removal. *Carbohydr. Polym.* **2017**, *175*, 584–591.

(10) King, J. F.; Szczuka, A.; Zhang, Z.; Mitch, W. A. Efficacy of ozone for removal of pesticides, metals and indicator virus from reverse osmosis concentrates generated during potable reuse of municipal wastewaters. *Water Res.* **2020**, *176*, No. 115744.

(11) Tawade, A. K.; Mohan Kumar, D.; Talele, P.; Sharma, K. K. K.; Tayade, S. N. Flower-Like ZnO-Decorated Polyaniline–Graphene oxide nano-composite for electrochemical oxidation of imidacloprid: A hybrid nanocomposite sensor. *J. Electron. Mater.* **2019**, *48*, 7747–7755.

(12) Heng, H. M.; Yang, J. P.; Yin, Y. J.; Meng, P. C.; Liu, X. Effect of precursor types on the performance of polyimide: A metal-free visible-light-driven photocatalyst for effective photocatalytic degradation of pollutants. *Catal. Today* **2020**, *340*, 225–235.

(13) Gegegel, C.; Simsek, U. B.; Gozmen, B.; Turabik, M. Comparison of MIL-101(Fe) and amine-functionalized MIL-101(Fe) as photocatalysts for the removal of imidacloprid in aqueous solution. *Journal of the Iranian Chemical Society* **2019**, *16*, 1735–1748.

(14) Mousavi, M.; Habibi-Yangjeh, A.; Pouran, S. R. Review on magnetically separable graphitic carbon nitride-based nanocomposites as promising visible-light-driven photocatalysts. *Journal of Materials Science: Materials in Electronics* **2018**, *29*, 1719–1747.

(15) Wang, S.; Liu, Y.; Wang, J. Peroxymonosulfate Activation by Fe–Co–O-Codoped Graphite Carbon Nitride for Degradation of Sulfamethoxazole. *Environ. Sci. Technol.* **2020**, *54*, 10361–10369.

(16) Cao, D.; Sha, Q.; Wang, J.; Li, J.; Ren, J.; Shen, T.; Bai, S.; He, L.; Song, Y.-F. Advanced Anode Materials for Sodium-Ion Batteries: Confining Polyoxometalates in Flexible Metal–Organic Frameworks by the “Breathing Effect. *ACS Appl. Mater. Interfaces* **2022**, *14* (19), 22186–22196.

(17) Cheng, P.; Wang, C.; Kaneti, Y. V.; Eguchi, M.; Lin, J.; Yamauchi, Y.; Na, J. Practical MOF Nanoarchitectonics: New Strategies for Enhancing the Processability of MOFs for Practical Applications. *Langmuir* **2020**, *36*, 4231–4249.

(18) Wang, Q.; Wang, L.; Zheng, S.; Tan, M.; Yang, L.; Fu, Y.; Li, Q.; Du, H.; Yang, G. The strong interaction and confinement effect of Ag@ NH₂-MIL-88B for improving the conversion and durability of photocatalytic Cr (VI) reduction in the presence of a hole scavenger. *J. Hazard. Mater.* **2023**, *451*, No. 131149.

(19) Alluhaybi, A. A.; Alharbi, A.; Alshammari, K. F.; El-Desouky, M. G. Efficient Adsorption and Removal of the Herbicide 2, 4-Dichlorophenylacetic Acid from Aqueous Solutions Using MIL-88(Fe)-NH₂. *ACS omega* **2023**, *8* (43), 40775–40784.

(20) Wu, Q.; Yang, H.; Kang, L.; Gao, Z.; Ren, F. Fe-based metal-organic frameworks as Fenton-like catalysts for highly efficient degradation of tetracycline hydrochloride over a wide pH range:

acceleration of Fe(II)/Fe(III) cycle under visible light irradiation. *Appl. Catal. B Environ* **2020**, *263*, No. 118282.

(21) Zhao, F.; Liu, Y.; Hammouda, S. B.; Doshi, B.; Guijarro, N.; Min, X.; Tang, C.-J.; Sillanpää, M.; Sivula, K.; Wang, S. MIL-101(Fe)/g-C₃N₄ for enhanced visible-light-driven photocatalysis toward simultaneous reduction of Cr(VI) and oxidation of bisphenol A in aqueous media. *Appl. Catal., B* **2020**, *272*, No. 119033.

(22) Yi, J.; Wu, K.; Wu, H.; Guo, J.; Zhang, L.; Li, H.; Li, J. Synthesis of Novel g-C₃N₄/NH₂-MIL-88B (Fe) Composite Photocatalysis for Efficient Ciprofloxacin Degradation Under Simulated Sunlight Irradiation. *Nano* **2021**, *16* (06), 2150063.

(23) Dao, X. Y.; Xie, X. F.; Guo, J. H.; Zhang, X. Y.; Kang, Y. S.; Sun, W. Y. Boosting Photocatalytic CO₂ Reduction Efficiency by Heterostructures of NH₂-MIL-101(Fe)/g-C₃N₄. *ACS Applied Energy Materials* **2020**, *3* (4), 3946–3954.

(24) Xiang, Q.; Yu, Z.; Li, X.; Wang, P.; He, N.; Pang, Y.; Wang, Q.; Liu, Y. Construction of a highly stable gC 3 N 4/NH 2-MIL-88B (Fe)/CD@ graphene oxide self-cleaning membrane for dye wastewater separation and degradation. *New J. Chem.* **2022**, *46* (36), 17438–17455.

(25) Bezerra, M. A.; Santelli, R. E.; Oliveira, E. P.; Villar, L. S.; Escalera, L. A. response surface methodology (RSM) as a tool for optimization in analytical chemistry. *Talanta* **2008**, *76*, 965–977.

(26) Bruns, R.; Scarmino, I.; de, B.; neto, B. (2008). *statistical design—chemometrics*, 1st edn. (Elsevier: Amsterdam), p 422.

(27) Barghi, B.; Jürisoo, M.; Volokhova, M.; Seinberg, L.; Reile, I.; Mikli, V.; Niidu, A. Process Optimization for Catalytic Oxidation of Dibenzothiophene over UiO-66-NH₂ by Using a Response Surface Methodology. *ACS Omega* **2022**, *7*, 16288–16297.

(28) Kumar, A.; Shende, D.; Wasewar, K. Central composite design approach for optimization of levulinic acid separation by reactive components. *Ind. Eng. Chem. Res.* **2021**, *60* (37), 13692–13700.

(29) Sarrai, A.; Hanini, S.; Merzouk, N.; Tassalit, D.; Szabó, T.; Hernádi, K.; Nagy, L. Using Central Composite Experimental Design to Optimize the Degradation of Tylosin from Aqueous Solution by Photo-Fenton Reaction. *Materials* **2016**, *9* (6), 428.

(30) Wan, Z.; Zhang, G.; Wu, X.; Yin, S. Novel visible-light-driven Z-scheme Bi₁₂GeO₂₀/g-C₃N₄ photocatalyst: Oxygen-induced pathway of organic pollutants degradation and proton assisted electron transfer mechanism of Cr (VI) reduction. *Appl. Catal., B* **2017**, *207*, 17–26.

(31) Chen, M.-L.; Lu, T.-H.; Long, L.-L.; Xu, Z.; Ding, L.; Cheng, Y.-H. NH₂-Fe-MILs for effective adsorption and Fenton-like degradation of imidacloprid: Removal performance and mechanism investigation. *Environ. Eng. Res.* **2022**, *27* (2), 200702 DOI: 10.4491/ eer.2020.702.

(32) Bauer, S.; Serre, C.; Devic, T.; Horcajada, P.; Marrot, J.; Férey, G.; Stock, N. High-throughput assisted rationalization of the formation of metal organic frameworks in the iron (III) aminoterephthalate solvothermal system. *Inorganic chemistry* **2008**, *47* (17), 7568–7576.

(33) Liu, C.; Wu, Q.; Ji, M.; Zhu, H.; Hou, H.; Yang, Q.; Jiang, C.; Wang, J.; Tian, L.; Chen, J.; Hou, W. Constructing Z-scheme charge separation in 2D layered porous BiOBr/graphic C₃N₄ nanosheets nonjunction with enhanced photocatalytic activity. *J. Alloys Compd.* **2017**, *723*, 1121–1131.

(34) Wang, Y.; Tan, G.; Liu, T.; Su, Y.; Ren, H.; Zhang, X.; Xia, A.; Lv, L.; Liu, Y. Photocatalytic properties of the g-C₃N₄/{010} facets BiVO₄ interface Z-Scheme photocatalysts induced by BiVO₄ surface heterojunction. *Appl. Catal., B* **2018**, *234*, 37–49.

(35) Golmohamadpour, A.; Bahramian, B.; Shafiee, A.; Ma’mani, L. Slow released delivery of alendronate using β-cyclodextrine modified Fe–MOF encapsulated porous hydroxyapatite. *Journal of Inorganic and Organometallic Polymers and Materials* **2018**, *28*, 1991–2000.

(36) Mohammadi Rasooli, M.; Sepehrmansourie, H.; Zarei, M.; Zolfogol, M. A.; Hosseinfard, M.; Gu, Y. Catalytic Application of Functionalized Bimetallic–Organic Frameworks with Phosphorous acid Tags in the Synthesis of Pyrazolo [4, 3-e] pyridines. *ACS omega* **2023**, *8* (28), 25303.

- (37) Zango, Z. U.; Jumbri, K.; Sambudi, N. S.; Hanif Abu Bakar, N. H.; Fathihah Abdullah, N. A.; Basheer, C.; Saad, B. Removal of anthracene in water by MIL-88 (Fe), NH₂-MIL-88 (Fe), and mixed-MIL-88 (Fe) metal–organic frameworks. *RSC Adv.* **2019**, *9* (71), 41490–41501.
- (38) Hu, X.; Wang, H.; Qi, S.; Su, Z.; Wang, J.; Chen, K.; Xie, A. Co/C nanomaterial derived from Co metal–organic framework for oxygen evolution reaction. *Ionic* **2022**, 813–821.
- (39) Yi, X.; He, X.; Yin, F.; Yang, T.; Chen, B.; Li, G. NH₂-MIL-88B-Fe for electrocatalytic N₂ fixation to NH₃ with high Faradaic efficiency under ambient conditions in neutral electrolyte. *J. Mater. Sci.* **2020**, *55*, 12041–12052.
- (40) Lima, M. J.; Silva, A. M. T.; Silva, C. G.; Faria, J. L. thermal, chemical and mechanical processes as metal-free photocatalyst for the selective synthesis of benzaldehyde from benzyl alcohol. *J. Catal.* **2017**, *353*, 44–53.
- (41) Shao, L.; Yu, Z.; Li, X.; Li, X.; Zeng, H.; Feng, X. Carbon nanodots anchored onto the metal-organic framework NH₂-MIL-88B (Fe) as a novel visible light-driven photocatalyst: Photocatalytic performance and mechanism investigation. *Appl. Surf. Sci.* **2020**, *505*, No. 144616.
- (42) Sedaghati, N.; Habibi-Yangjeh, A.; Khataee, A. Fabrication of g-C₃N₄ nanosheet/Bi₅O₇Br/NH₂-MIL-88B (Fe) nanocomposites: Double S-scheme photocatalysts with impressive performance for the removal of antibiotics under visible light. *International Journal of Minerals, Metallurgy and Materials* **2023**, *30* (7), 1363–1374.
- (43) Huang, W.; Liu, N.; Zhang, X.; Wu, M.; Tang, L. Metal organic framework g-C₃N₄/MIL-53 (Fe) heterojunctions with enhanced photocatalytic activity for Cr (VI) reduction under visible light. *Appl. Surf. Sci.* **2017**, *425*, 107–116.
- (44) Li, J. J.; Cai, S. C.; Xu, Z.; Chen, X.; Chen, J.; Jia, H. P.; Chen, J. Solvothermal syntheses of Bi and Zn co-doped TiO₂ with enhanced electron-hole separation and efficient photodegradation of gaseous toluene under visible-light. *Journal of hazardous materials* **2017**, *325*, 261–270.
- (45) Fang, L. J.; Wang, X. L.; Li, Y. H.; Liu, P. F.; Wang, Y. L.; Zeng, H. D.; Yang, H. G. Nickel nanoparticles coated with graphene layers as efficient co-catalyst for photocatalytic hydrogen evolution. *Appl. Catal., B* **2017**, *200*, 578–584.
- (46) Kaur, M.; Mehta, S. K.; Devi, P.; Kansal, S. K. Bi₂WO₆/NH₂-MIL-88B (Fe) heterostructure: An efficient sunlight driven photocatalyst for the degradation of antibiotic tetracycline in aqueous medium. *Advanced Powder Technology* **2021**, *32* (12), 4788–4804.
- (47) Su, Q.; Li, J.; Yuan, H.; Wang, B.; Wang, Y.; Li, Y.; Xing, Y. Visible-light-driven photocatalytic degradation of ofloxacin by g-C₃N₄/NH₂-MIL-88B (Fe) heterostructure: Mechanisms, DFT calculation, degradation pathway and toxicity evolution. *Chemical Engineering Journal* **2022**, *427*, No. 131594.
- (48) Liu, B.; Wu, Y.; Han, X.; Lv, J.; Zhang, J.; Shi, H. Facile synthesis of g-C₃N₄/amine-functionalized MIL-101 (Fe) composites with efficient photocatalytic activities under visible light irradiation. *Journal of Materials Science: Materials in Electronics* **2018**, *29*, 17591–17601.
- (49) Lei, Z.-D.; Xue, Y.-C.; Chen, W.-Q.; Li, L.; Qiu, W.-H.; Zhang, Y.; Tang, L. The influence of carbon nitride nanosheets doping on the crystalline formation of MIL-88B(Fe) and the photocatalytic activities. *Small* **2018**, *14* (35), 1802045.
- (50) Hou, S.; Wu, Y. N.; Feng, L.; Chen, W.; Wang, Y.; Morlay, C.; Li, F. Green synthesis and evaluation of an iron-based metal–organic framework MIL-88B for efficient decontamination of arsenate from water. *Dalton transactions* **2018**, *47* (7), 2222–2231.
- (51) Sudhaik, A.; Raizada, P.; Singh, P.; Hosseini-Bandegharai, A.; Thakur, V. K.; Nguyen, V. H. Highly effective degradation of imidacloprid by H₂O₂/fullerene decorated P-doped g-C₃N₄ photocatalyst. *Journal of Environmental Chemical Engineering* **2020**, *8* (6), No. 104483.
- (52) Li, Y.; Jiang, J.; Fang, Y.; Cao, Z.; Chen, D.; Li, N.; Xu, Q.; Lu, J. TiO₂ nanoparticles anchored onto the metal–organic framework NH₂-MIL-88B (Fe) as an adsorptive photocatalyst with enhanced ferration-like degradation of organic pollutants under visible light irradiation. *ACS Sustainable Chem. Eng.* **2018**, *6* (12), 16186–16197.
- (53) Guo, H.; Niu, B.; Wu, X.; Zhang, Y.; Ying, S. Effective removal of 2, 4, 6-trinitrophenol over hexagonal metal–organic framework NH₂-MIL-88B (Fe). *Appl. Organomet. Chem.* **2019**, *33* (1), e4580.
- (54) Bai, C.; Bi, J.; Wu, J.; Meng, H.; Xu, Y.; Han, Y.; Zhang, X. Fabrication of noble-metal-free g-C₃N₄-MIL-53(Fe) composite for enhanced photocatalytic H₂-generation performance. *Appl. Organomet. Chem.* **2018**, *32* (12), 4597.
- (55) Liang, R.; Jing, F.; Shen, L.; Qin, N.; Wu, L. MIL-53 (Fe) as a highly efficient bifunctional photocatalyst for the simultaneous reduction of Cr (VI) and oxidation of dyes. *Journal of hazardous materials* **2015**, *287*, 364–372.
- (56) Lang, N.; Tuel, A. A fast and efficient ion-exchange procedure to remove surfactant molecules from MCM-41 materials. *Chemistry of materials* **2004**, *16* (10), 1961–1966.
- (57) Faisal, M.; Ahmed, J.; S.Algethami, J.; Jalalah, M.; Alsareii, S. A.; Alsaiani, M.; Harraz, F. A. Visible-light responsive Au nanoparticle-decorated polypyrrole-carbon black/SnO₂ ternary nanocomposite for ultrafast removal of insecticide imidacloprid and methylene blue. *J. Ind. Eng. Chem.* **2023**, *121*, 287–298.
- (58) Liang, F.; Zhang, Y. H.; He, B.; Yang, J.; Shi, Q.; Shi, F. N. Enhanced photocatalytic degradation of imidacloprid and RhB by the precursor derived Bi₁₂ 7Co₀. 3O₁₉. 35 under different pH value. *J. Phys. Chem. Solids* **2022**, *164*, No. 110638.
- (59) Kobkeatthawin, T.; Trakulmututa, J.; Amornsakchai, T.; Kajitvichyanukul, P.; Smith, S. M. Identification of Active Species in Photodegradation of Aqueous Imidacloprid over g-C₃N₄/TiO₂ Nanocomposites. *Catalysts* **2022**, *12* (2), 120.
- (60) Garg, R.; Gupta, R.; Bansal, A. Photocatalytic degradation of imidacloprid using semiconductor hybrid nano-catalyst: kinetics, surface reactions and degradation pathways. *Int. J. Environ. Sci. Technol.* **2021**, *18*, 1425–1442.
- (61) Babić, K.; Tomašić, V.; Gilja, V.; Le Cunff, J.; Gomzi, V.; Pintar, A.; Žerjav, G.; Kurajica, S.; Duplančić, M.; Zelić, I. E.; Pavičić, T. V.; Grčić, I. Photocatalytic degradation of imidacloprid in the flat-plate photoreactor under UVA and simulated solar irradiance conditions—The influence of operating conditions, kinetics and degradation pathway. *J. Environ. Chem. Eng.* **2021**, *9* (4), No. 105611.
- (62) Liang, F.; Lu, M.; Zhang, Y. H.; Shi, Q.; Shi, F. Journal Pre-proof Synthesis and structure of a bismuth-cobalt bimetal coordination polymer for green efficient photocatalytic degradation of organic wastes under visible light. *J. Mol. Struct.* **2021**, *1230*, No. 129636.
- (63) Adabavazeh, H.; Saljooqi, A.; Shamspur, T.; Mostafavi, A. Synthesis of polyaniline decorated with ZnO and CoMoO₄ nanoparticles for enhanced photocatalytic degradation of imidacloprid pesticide under visible light. *Polyhedron* **2021**, *198*, No. 115058.
- (64) Lee, Y.-J.; Kang, J.-K.; Park, S.-J.; Lee, C.-G.; Moon, J.-K.; Alvarez, P. J. J. Photocatalytic degradation of neonicotinoid insecticides using sulfate-doped Ag₃PO₄ with enhanced visible light activity. *Chem. Eng. J.* **2020**, *402*, No. 126183.
- (65) Merci, S.; Saljooqi, A.; Shamspur, T.; Mostafavi, A. WO₃ nanoplates decorated with polyaniline and CdS nanoparticles as a new photocatalyst for degradation of imidacloprid pesticide from water. *Environ. Sci. Pollut Res.* **2021**, *28*, 35764–35776.
- (66) Guo, D.; Zhu, X.; Chen, S.; Wang, C.; Pi, M.; Chen, X.; Shi, Y.; Dai, J. Ionic-Liquid-Assisted Hydrothermal Synthesis of Ag/AgBr for Photodegradation of Imidacloprid under Visible Light. *Clean: Soil, Air, Water* **2019**, 1900064–1900071.
- (67) El-Shafai, N. M.; El-Khouly, M. E.; El-Kemary, M.; Ramadan, M. S.; Derbalah, M. S.; Masoud, J. Fabrication and characterization of graphene oxide–titanium dioxide nanocomposite for degradation of some toxic insecticides. *Indus and Eng. Chem.* **2019**, *69*, 315–323.
- (68) Soltani-nezhad, F.; Saljooqi, A.; Shamspur, T.; Mostafavi, A. Photocatalytic degradation of imidacloprid using GO/Fe₃O₄/TiO₂ – NiO under visible radiation: Optimization by response level method. *Polyhedron* **2019**, *165*, 188–196.

(69) Naghizadeh, M.; Taher, M. A.; Tamaddon, A.-M. Facile synthesis and characterization of magnetic nanocomposite ZnO/CoFe₂O₄ hetero-structure for rapid photocatalytic degradation of imidacloprid. *Heliyon* **2019**, *5*, e0287.

(70) Akbari Shorgoli, A.; Shokri, M. Photocatalytic Degradation of Imidacloprid Pesticide in Aqueous Solution by TiO₂ Nanoparticles Immobilized on the Glass Plate. *Chem. Eng. Commun.* **2017**, *204* (9), 1061–1069.

(71) Liu, X.; Wu, X.; Long, Z.; Zhang, C.; Ma, M.; Hao, X.; Zhang, H.; Pan, C. Photodegradation of Imidacloprid in Aqueous Solution by the Metal-Free Catalyst Graphitic Carbon Nitride using an Energy-Saving Lamp. *J. Agric. Food Chem.* **2015**, *63* (19), 4754–476.